In Situ Surface Reconstruction of Catalysts for Enhanced Hydrogen Evolution

Yingbo Zhang [†], Junan Pan [†], Gu Gong, Renxuan Song, Ye Yuan, Mengzhu Li, Weifeng Hu, Pengcheng Fan, Lexing Yuan and Longlu Wang *

College of Electronic and Optical Engineering & College of Flexible Electronics (Future Technology), Nanjing University of Posts & Telecommunications (NJUPT), 9 Wenyuan, Nanjing 210023, China
* Correspondence: wanglonglu@njupt.edu.cn
† These authors equally to this work.

Abstract: The in situ surface reconstitution of a catalyst for hydrogen evolution refers to its structure evolution induced by strong interactions with reaction intermediates during the hydrogen evolution reaction (HER), which eventually leads to the self-optimization of active sites. In consideration of the superior performance that can be achieved by in situ surface reconstitution, more and more attention has been paid to the relationship between active site structure evolution and the self-optimization of HER activity. More and more in situ and/or operando techniques have been explored to track the dynamic structural evolution of HER catalysts in order to clarify the underlying mechanism. This review summarizes recent advances in various types of reconstruction such as the reconfiguration of crystallinity, morphological evolution, chemical composition evolution, phase transition refactoring, surface defects, and interface refactoring in the HER process. Finally, different perspectives and outlooks are offered to guide future investigations. This review is expected to provide some new clues for a deeper understanding of in situ surface reconfiguration in hydrogen evolution reactions and the targeted design of catalysts with desirable structures.

Keywords: surface reconstitution; self-optimization; dynamic structural evolution; underlying mechanism; hydrogen evolution reaction

1. Introduction

In situ surface reconstruction is a phenomenon in which the structure of the active center of a catalyst spontaneously evolves during the catalytic process or evolves with a strong interaction between the catalyst and the reaction intermediates under the influence of certain catalytic environments due to the reactive mechanism of the catalysts involved in the reaction. The ultimate catalytic performance can be self-optimized by virtue of in situ reconstruction, which is an important method for designing highly active and efficient catalysts [1–5]. Various new structures can be derived from different types of in situ surface reconstruction, and active site structure evolution phenomena, such as morphology evolution [6–8], phase transition [9,10], and defect introduction [11,12], have attracted attention from both theoretical and experimental perspectives [13]. Therefore, it is essential to reveal the evolution of the active site structure at the molecular or even atomic level to deeply clarify the catalytic mechanism and further develop cost-effective catalysts with desirable catalytic performance [14]. In particular, in the field of HER catalysts, a large number of studies have focused on the characterization of catalyst structures before and after reactions while ignoring the possible dynamic evolution occurring during the reaction process. Due to temporal and spatial mismatch, it cannot be conclusively proved that the physical structure and chemical components of catalysts are exactly as the same during and after the reaction. Accordingly, it is hard to describe the real active site structure for the HER.

In recent years, with advancements in in situ and/or operando techniques [15–17], more and more researchers have highlighted the importance and prevalence of the in situ reconstitution of HER catalysts. In situ characterization has become an indispensable characterization method in catalytic reactions that not only helps us to further explore the catalytic mechanism but also allows for outstanding contributions to the further design of various effective catalysts. In situ infrared, in situ Raman, in situ X-ray photoelectron spectroscopy (XPS), and in situ synchrotron radiation have been widely used. For example, Qiu et al. reported that NiFe-layered double hydroxides were found to have improved crystallinity by means of in situ characterization during the electrolysis of water under alkaline conditions, and this resulted in a lower charge transfer resistance [18]. Similarly, Zou and colleagues found that ferrous sulfide nanosheet arrays prepared via the direct sulfidation of iron foam with thiourea could gradually generate $Fe@FeO_xS_y$ nanoparticles, which acted as new active sites and thus enhanced their catalytic activity over time as the HER proceeded [19]. Homoplastically, our group reported and demonstrated the irreversible phase change of $1T\text{-}MoS_2$ to $1T'\text{-}MoS_2$ during the photocatalytic HER, confirming the occurrence of self-optimization in the HER process [20].

Understanding and applying the formation mechanism and impact of in situ surface reconstruction is a very important strategy to solve energy and resource problems [14]. This review summarizes the in situ reconstruction of catalysts during HERs, including the reconfiguration of crystallinity, morphology evolution, chemical composition evolution, phase transition, and introduced surface defects (as shown in Figure 1), as well as how they affect catalytic performance. Finally, this review provides some perspectives that are expected to be meaningful for future catalyst design and development.
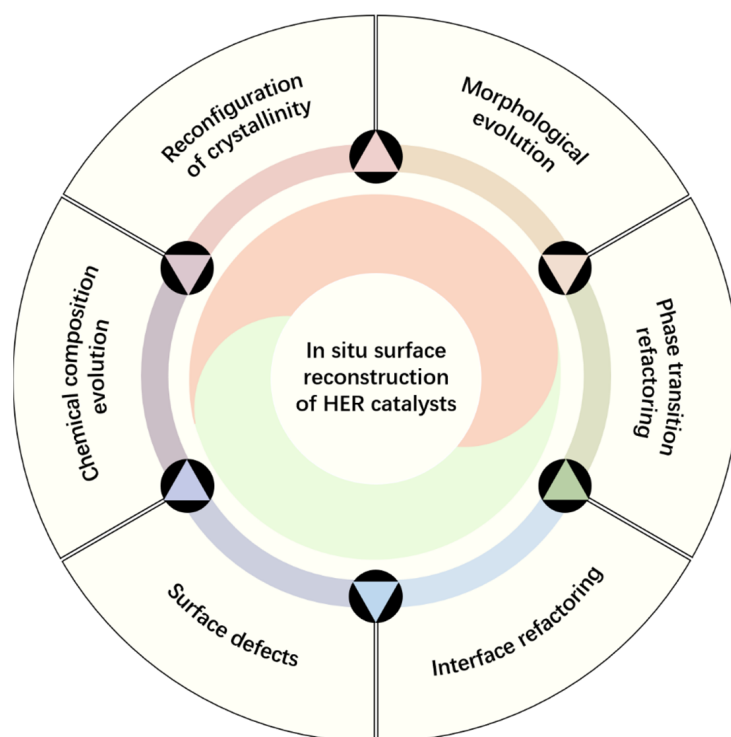
Figure 1. Schematic diagram of the in situ surface reconstruction of HER catalysts.

2. Reconfiguration Types

In recent years, with the increasing interest in HER catalysts, non-noble metal-based HER catalysts, such as TMD (transition metal disulfide), TMN (transition metal nitride), and TMC (transition metal carbides) [21–24], have been developed at an unprecedented speed due to their abundant Earth abundance, low cost and superior performance. Although the catalytic performance of these catalysts has been reported to be comparable to that of

Pt/C electrodes, there is still a lack of deep insight into the surface in situ reconstitution phenomena that occur during the catalytic process. Nowadays, in situ reconstitution has been reported to affect the catalytic activity and stability of catalysts [25–27], and catalysts for the HER have been shown to have a period of activation for enhancing catalytic performance. In other words, it is theoretically possible to achieve the self-optimization of HER catalyst performance through certain in situ reconfiguration designs. Here, we highlight five types of in situ reconfiguration phenomena, namely, crystallinity change, morphology evolution, chemical component change, phase reconfiguration, and defects, from the physical structure and chemical composition perspectives. Some of these phenomena are induced by strong interactions between catalyst surface atoms and reaction intermediates, while others are self-structural changes caused by specific catalytic conditions. In this section, we focus on latest processes of in situ surface reconstruction phenomena and establish a connection between changes in the structure of an active site center and the self-optimization of its performance, aiming to provide a solid foundation for the further design of excellent HER catalysts.

2.1. Reconfiguration of Crystallinity

The change in crystallinity during catalytic reactions has been shown to be one of the reasons for the improvement in catalyst performance. Qiu et al. discovered the phenomena of the in situ reconstitution of NiFe-layered double hydroxides (LDHs) during the electrolysis of water under alkaline conditions [18]. The performance of NiFe-layered double hydroxides was evaluated at 1.7 V for 100 h in a base electrolyte at room temperature. As shown in Figure 2A, the reacted sample (named H-NiFe LDH) required only -59 mV of overpotential to achieve a current density of 10 mA cm^{-2}, which is more than twice the performance of NiFe LDH. This was confirmed by the relatively low Tafel slope shown in the figure, with a value of 62.30 mV dec^{-1} implying that H-NiFe LDH has a good conductivity and a low activity barrier. The authors further characterized H-NiFe LDHs after ruling out the possibility of changes in catalyst performance by nickel foam, inspired by previous reports on the increase in aging Ni(OH)$_2$ activity [28,29]. The SAED (selected area electron diffraction) results (Figure 2B) revealed that the crystal plane spacing was 0.15 nm, corresponding to the nickel (113) and bicarbonate iron (113) planes, indicating that the catalyst crystal structure did not change over the course of the reaction. Notably, the sharpness of the ring pattern significantly increased from left to right, which indicated an increase in the crystallinity of the catalyst during the reaction. This facilitated the charge transport in the reaction by reducing the reaction resistance. Concomitant with the change in crystallinity was the valence increases. In the Ni XPS results shown in Figure 2C,D, the relative increase in peaks in the Ni p spectra and the accompanying broadening of the total peaks indicate the valence increase in Ni. For the O 1s spectra, the increase in peaks at higher energies (~531 eV) also implies an increase in the amount of O bound to higher valence elements. To further investigate the interfacial active phase of the catalyst, in situ Raman tests were performed on the catalyst samples (Figure 2E). Energy bands from 400 cm^{-1} to 600 cm^{-1} confirmed the presence of metal–oxygen vibrations for FeOOH (Fe^{3+}) and Ni(OH)$_2$. Additionally, combining XPS and Raman data revealed that the presence of Fe could inhibit the electrochemical self-reduction activity of Ni compounds, which consequently promoted the dissociation of water. That is, the formed substances (H$_{ad}$-NiO and OH$_{ad}$-FeO) were compatible with the water dissociation step (Volmer reaction), which could greatly improve the efficiency of the hydrolysis reaction (Figure 2G). It was the synergistic effect of better H$_{ad}$ adsorption capacity and a good electron transfer rate that led to a significant improvement in the HER activity of the NiFe LDH. It appears that the reconfiguration of crystallinity in the HER process tends to result in a better charge transfer rate for the catalyst, which consequently further reduces reaction resistance and leads to the self-optimization of catalytic activity.
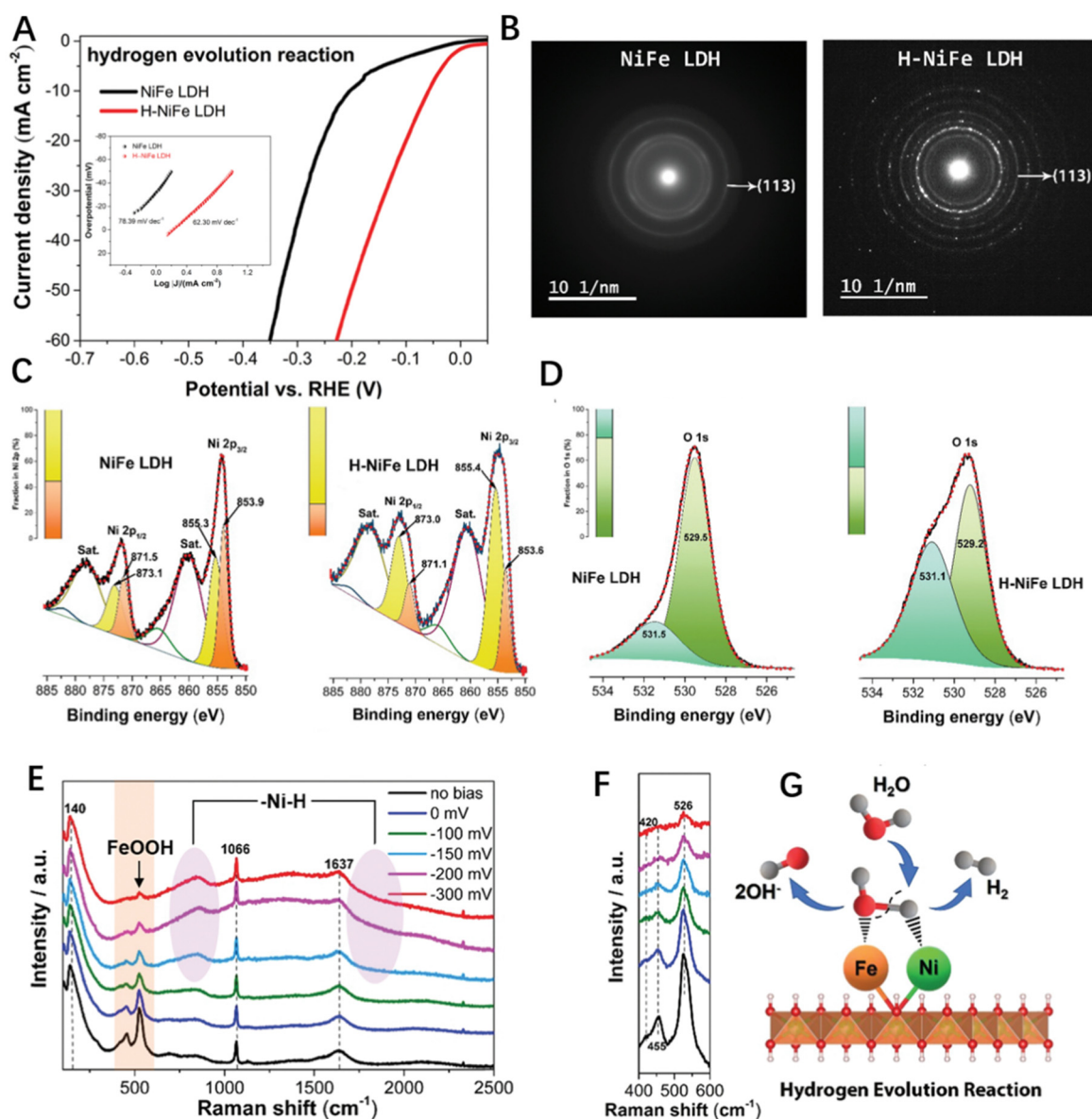
Figure 2. (**A**) Polarization curves obtained for pristine NiFe and H-NiFe LDHs in a three-electrode structure with a 1 M KOH aqueous electrolyte at a scan rate of 5 mV s^{-1}. The inset plots are Tafel plots with 100% iR compensation for both at the abovementioned conditions. (**B**) SAED plots of NiFe and H-NiFe LDHs. High-resolution XPS patterns of Ni 2p (**C**) and O 1s (**D**) in NiFe and H-NiFe LDHs. (**E**) In situ Raman spectroscopy test results of NiFe LDH in the large wave number region during the HER in the 1 M KOH environment at different overpotentials. (**F**) The amplification of the orange region in (**E**). (**G**) Diagram of the reaction mechanism of NiFe LDH in the HER process. Reproduced with permission from [18], ©The Royal Society of Chemistry 2014.

2.2. Morphological Evolution

With the development of in situ characterization techniques and the in-depth investigation of the dynamics of catalysts during hydrogen precipitation reactions, morphology evolution (a phenomenon that often occurs in catalysts during HERs) has gained much attention due to its ability to generate under-liganded active sites and thus enhance catalyst activity. Compared with more complex methods of optimizing the design of HER catalysts, morphological evolution offers advantages in terms of achieving higher catalytic activity with minimal additional processing. Recently, the morphological evolution of H-TaS$_2$ during HERs was intensively investigated with microscopic analysis and EIS tests [30]. The AFM results (Figure 3A,B) showed that the flakes became smaller, thinner and more

dispersed compared with the pre-cycling period. This was also confirmed by the results of the statistical thickness distribution before and after cycling (Figure 3C,D), which showed an increase in the number of flakes with thicknesses in range from 100 nm to 300 nm. This morphological evolution led to two favorable results for H-TaS$_2$. First, the interlayer electron transfer pathway was shortened due to the thinning of the experimental sample. For weakly bound layered materials in general, the electron transfer efficiency in the stacking direction tended to be poor, and the test results of the effective capacitance, charge transfer resistance, and fragmentation cycle changes (Figure 3E) showed that the post-cycle morphology evolution decreased its charge transfer resistance. The increase in conductivity implied that the interlayer charge transfer became easier, suggesting that the reaction rate-determining step deviated from the initial electron transfer (Volmer reaction) process. Second, the increase in effective bilayer capacitance (as shown in Figure 3E) suggested that this morphological evolution improved the accessibility of water protons to the active basal sites, thereby increasing the effective active surface area. Thus, the increase in conductivity synergistically contributed to the overall catalyst performance with the accessible surface area. To facilitate understanding, a schematic diagram of the morphological evolution mechanism was presented (Figure 3F). It was the precipitation of hydrogen bubbles at the basal sites of the stacked layer that led to the perforation and exfoliation of the sample, which consequently led to an increasing catalyst performance as the reaction proceeded.
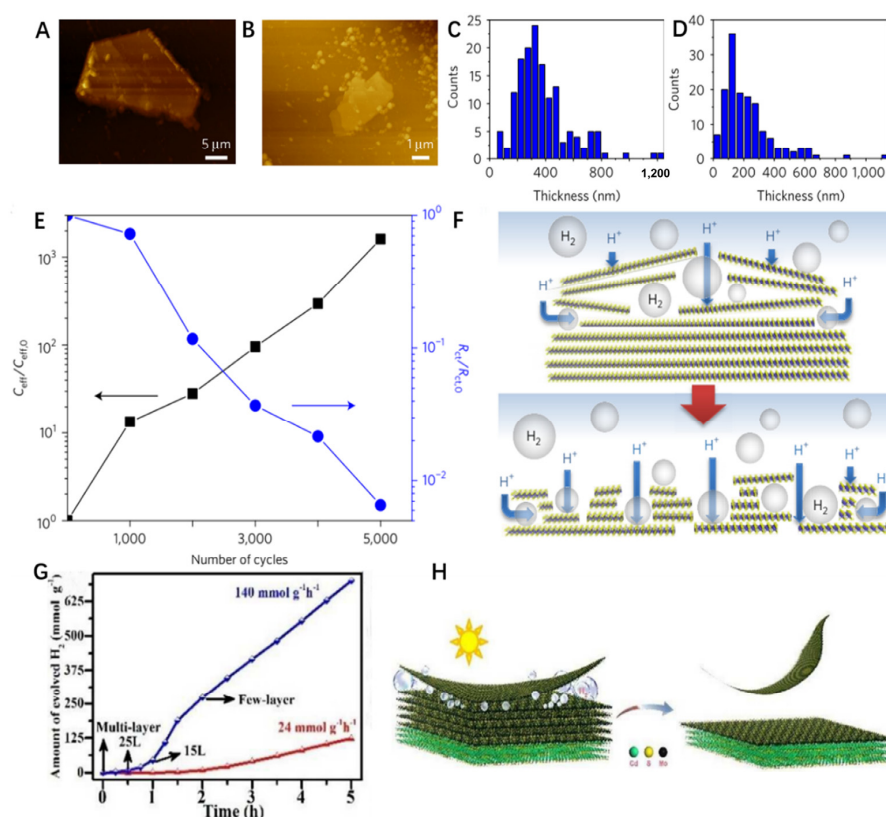
Figure 3. AFM images of H-TaS$_2$ before (**A**) and after (**B**) the reaction. (**C,D**) Statistical thickness distributions of H-TaS$_2$ before and after the reaction, respectively. (**E**) Variations of effective capacitance ($C_{eff}/C_{eff,0}$, where 0 is the initial value) and charge transfer resistance ($R_{ct}/R_{ct,0}$) with cycling. (**F**) Schematic diagram of the mechanism of the morphological evolution process. The flat plate represents the MX$_2$ layer, and the sphere represents the H$_2$ bubble generated during the HER. Reproduced with permission from [30], ©Springer Nature 2017. (**G**) Photocatalytic hydrogen production performance of vdWHs under high (red line) and low (blue line) pressure conditions. (**H**) Schematic diagram of the process principle based on bubble exfoliation to prepare highly active MoS$_2$/CdS vdWHs. Reproduced with permission from [31], ©The Royal Society of Chemistry 2014.

In addition, S. lqbal and colleagues discovered that the H_2 bubbles generated in the photocatalytic HER process could exfoliate MoS_2 layer by layer, and they applied this mechanism to the in situ preparation of multilayer MoS_2/CdS van der Waals heterostructures for enhanced photocatalytic hydrogen precipitation [31]. Figure 3G shows that the experimentally obtained samples showed self-optimized performance, as demonstrated by the increase in the average H_2 production rate from 27 mmol $g_{(CdS)}^{-1}$ h^{-1} in the first hour to 140 mmol $g_{(CdS)}^{-1}$ h^{-1} with AQY (apparent quantum yield) of 66% at 420 nm after two hours, which was higher than that of the recently reported photocatalytic hydrogen production system based on MoS_2/CdS photocatalysts [32,33]. Based on these experimental results, a process based on the precipitation of H_2 bubbles leading to the interlayer exfoliation of the sample and thus the preparation of highly active MoS_2/CdS vdWHs was proposed, as shown in Figure 3H. Under the high H_2 bubble growth rate, the Van der Waals forces between the MoS_2 nanocrystal layers were weakened, and the layers were exfoliated into several layers. These experiments revealed the existence of morphological evolution during the HER process, i.e., the high growth rate of H_2 bubbles during the reaction caused the perforation and even the interlayer exfoliation of the sample, as well as providing new ideas and methods to guide the preparation of self-optimized, highly active catalysts.

2.3. Chemical Composition Evolution

A catalyst works by participating in a unit step that changes the reaction rate by changing the activation energy of the reaction. During electrocatalytic hydrogen evolution, the reaction pathway of catalysts is highly sensitive to the characteristics of the active center and local reaction environment, which leads to the evolution of chemical components in some catalysts.

2.3.1. Complete Species Transition

Zou and colleagues analyzed the HER catalytic process of ferrous sulfide nanosheet arrays grown on iron foam prepared by the direct sulfurization of iron foam with thiourea in a solvothermal system, and they reported an ultra-high catalytic activity for the HER [19]. For the convenience of expression, the sample catalyzed by the HER was called Fe-H_2cat. As shown in Figure 4A, both IF (iron foam) and FeS/IF were relatively inactive in the HER, while the current densities of Fe-H_2cat reached 100 mA cm^{-2} and 1000 mA cm^{-2} (without rectification) at 300 mV and 510 mV of overpotential, respectively. Moreover, it was noteworthy that the catalytic activity of Fe-H_2cat was much higher than that of Pt/C in the wide current density range above 300 mA cm^{-2}. After correcting the original iR loss data (Figure 4B), Fe-H_2cat only needed 243 mV and 336 mV of overpotential to achieve current densities of 100 mA cm^{-2} and 1000 mA cm^{-2}, respectively. This indicated that the catalyst changed during the reaction, and the catalyst was further characterized following this idea. SEM images (Figure 4C) showed that the array structure of the FeS/IF nanosheets was almost intact in Fe-H_2cat, and a large number of nanoparticles with sizes of 10–20 nm appeared on the surface of the FeS nanosheets. It was reported that the formed iron nanoparticles could be rapidly partially oxidized in an aerobic environment and that a thin crust of ferric oxide appeared around the nanoparticles [34]. This structure was found to have many advantages, and it was the integration of these advantages that led to the good catalytic performance of Fe-H_2cat, as shown in Figure 4D. First, because FeS is inherently metallic (or conductive) and electrically connected to a metal collector (i.e., IF), FeS/IF could act as a 3D scaffold, ensuring that external electrons were readily available to all catalytically active phases (i.e., Fe@FeOxSy). Additionally, the use of 3D iron foam was able to increase the catalyst load per geometric area and improve the mass transfer performance. In addition, polymer adhesives were typically required for electrically driven catalysts such as powdered Pt/C catalysts, and the direct fixation of each Fe@FeO$_x$S$_y$ nanoparticle to the conductive FeS nanosheet eliminated the need for polymer adhesives and reduced the interfacial resistance between them, thus improving the structure and catalytic stability of the electrode. Finally, this unique structure enabled Fe-H_2cat to have

an underwater superhydrophobic surface and thus excellent mass transfer performance. Next, an S/O-covered Fe (111) surface was constructed as a theoretical model to better understand the synergistic enhancement mechanism of the O and S binary nonmetals of Fe@FeO$_x$S$_y$ (Figure 4E), and a model of O-covered Fe (111) surface was constructed for comparison (Figure 4F). The authors evaluated the free energy of voltametric H* ($\triangle G_{H*}$) on two surfaces of all possible adsorption locations (Figure 4G). Obviously, compared with the O-covered Fe surface and FeS, the S/O-covered Fe surface had a smaller $\triangle G_{H*}$ value, that is, the S/O-covered Fe surface constituted a more efficient catalytic active center, which was consistent with the experimental results.
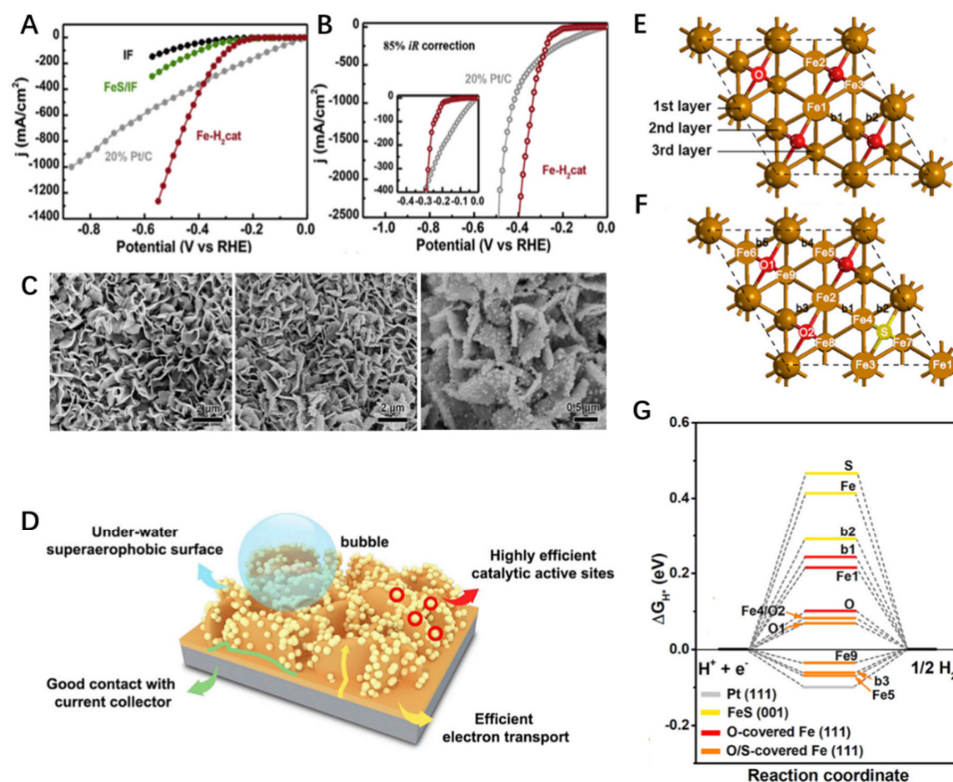
Figure 4. (**A**) Linear sweep voltammetry (LSV) curves of the HER against IF, Pt/C (20 wt %), Fe-H$_2$cat and FeS/IF in a 1 M KOH solution (without iR correction). (**B**) LSV curves of Fe-H$_2$cat with Pt/C (20 wt %) corrected with 85% iR for the HER. (**C**) From left to right, SEM images of Fe-S/IF, low-magnification SEM images of Fe-H$_2$cat, and high-magnification SEM images of Fe-H$_2$cat. (**D**) Schematic of the principle of the HER activity enhancement of Fe-H$_2$cat. (**E**) Possible H* adsorption locations on the O-covered Fe (111) surface and (**F**) O/S-covered Fe (111) surface. All top positions on the surface (indicated by elemental symbols) and top shallow bridge positions (indicated by "b") are considered. (**G**) Calculated free energy diagrams for Pt (111), FeS (001), O-covered Fe (111), and O/S-covered Fe (111) surfaces at equilibrium potential for the HER. Reproduced with permission [19], Copyright 2018, Elsevier.

2.3.2. In Situ Surface Hydrogenation

Similarly, in situ hydrogenation, as an integral part of chemical composition evolution during in situ surface reconstruction, is considered a promising way to improve the visible light absorption and photocatalytic activity of semiconductor photocatalysts [35]. Zhu et al. prepared ZnIn$_2$S$_4$ nanosheets with a low-temperature reflux method and then peeled them off using a water-assisted surfactant/interlace-free stripping process [36]. Next, the ZIS nanosheets were processed in sealed quartz glass with Na$_2$S/Na$_2$SO$_3$ as the sacrificial agent under UV–visible light. In the first four hours of the experiment, the H$_2$ precipitation rate gradually increased with the increase in illumination time, and the color of ZIS changed from yellow to black within a few hours as the reaction progressed (Figure 5A). This indicated

that the HER performance of the ZIS nanosheets was self-optimized within the first four hours. Then, the ZIS nanosheets (H_xZIS-6 h) were measured with solid state nuclear magnetic resonance (NMR). The peaks at 3.35 and 4.0 PPM in the H-NMR spectrogram corresponded to S-H bonds (Figure 5B). The XPS spectrogram of the S 2P of H_xZIS-6 h (Figure 5C) shows that there were two types of sulfur (original sulfur and hydrogenated sulfur) in the sample, which was consistent with the signals of two S-H bonds corresponding to the two peaks mentioned above. It was further confirmed that part of the sulfur in the ZIS structure was hydrogenated during the reaction. Diffuse UV–visible spectroscopy (UV–vis) was used to characterize the intrinsic optical properties of the original and illuminated samples (Figure 5D). It is worth noting that all samples showed a fairly high absorbance in the UV and blue regions (<400 nm). The color changes indicated the presence of appropriate modifications in the crystal structure and the electronic structure, which might have been related to the hydrogen adsorbed on the surface of ZIS in the hydrogen evolution reaction, and also indicated the absorption range of visible light following in situ hydrogenation. In addition, the structural changes of the ZIS nanosheets during hydrogenation were investigated with DFT calculations. Figure 5E,F, respectively, shows the atomic structure of the original ZIS sample and the H_xZIS sample. The DOS (density of states) diagram of the original ZIS sample (Figure 5G) shows that the original ZIS had certain bandgap semiconductor characteristics. However, as shown in the atomic structure diagram and the DOS diagram of H_xZIS sample (Figure 5F,H), H was adsorbed on the surface and inserted into the inner surface layer. H adsorption significantly changed the DOS distribution and Fermi energy level, which reflected the complete charge transfer of H adsorption. It also indicated that the H_xZIS samples had zero band gap metal properties. In short, these results reflected the phenomena of the in situ surface reconstruction of ZIS nanosheets via in situ hydrogenation engineering during general UV–vis induced hydrogenation. These studies aid our understanding of the evolution of chemical components in in situ reconstruction phenomena and provide us with new inspiration for the design of new catalysts.
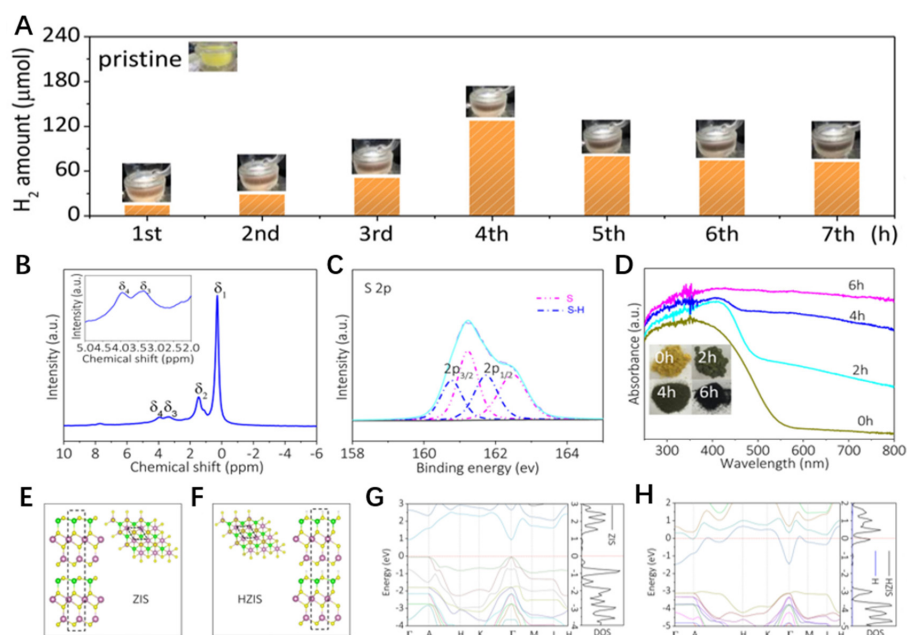
Figure 5. (**A**) Hydrogen content and corresponding color change of ZIS nanosheets at different time periods during the reaction. (**B**) H^1 solid-state NMR spectra of H_xZIS-6 h nanosheets. δ3 and δ4 are the signals of the S-H bonds; δ1 and δ2 are the signals of the adsorbed water molecules. (**C**) XPS spectrum of S 2p of H_xZIS-6 h. (**D**) UV–vis DRS spectra and photos of ZIS nanosheets at different time periods during the reaction. Top (**E**) and side (**F**) views of relaxed pristine ZIS systems and H_xZIS systems. (**G,H**) Electronic density of states of typical pristine ZIS systems and H_xZIS systems (DOS). Reproduced with permission [36], Copyright 2019, Elsevier.

2.3.3. In Situ Surface Oxygen Doping

Contrary to the abovementioned ways of achieving chemical component changes, the adjustment of surface electron density by means of heteroatom doping is also considered an important strategy to achieve the self-optimization of properties in in situ surface reconstructions. In a recent report, our group proposed an effective photon-induced strategy for the in situ oxygen doping of MoS_2 nanosheets in a low-oxygen environment and experimentally found that the intrinsically flexible MoS_2 nanosheets exhibited self-optimization of properties under low-oxygen conditions [37]. The performance of the intrinsically flexible MoS_2 nanosheets was found to be self-optimizing under the photocatalytic environment and moderate-oxygen conditions. The results of the real-time detection of the dynamic change of the H_2 generation rate under the condition of 1.2 mL of O_2 (Figure 6A) showed that the performance of MoS_2 could be self-optimized under the stimulation of O_2 for eight hours and finally reached its highest rate of 1.6 mmol h^{-1} g^{-1}. In other words, under moderate-O_2 conditions, MoS_2 underwent in situ oxygen doping and the activity of MoS_2 substrate was well-stimulated, showing efficient self-optimization performance. XPS spectra then confirmed the chemical composition change of the catalyst during the reaction. As shown in Figure 6B, the appearance of the O 1s peak at 530.6 eV, unlike the O 1s peak of pristine MoS_2 (532.0 eV), confirmed the formation of Mo-O bonds in S-O-MoS_2, i.e., the catalyst underwent in situ oxygen doping during the reaction. Raman spectroscopy tests were further used to reveal the type of bonding after O_2 activation [38,39]. As seen in Figure 6C, the peak intensities measured from S-O-MoS_2 were much weaker than those of pristine MoS_2, indicating that the long-range ordering of the 2H structure of MoS_2 was highly distorted due to oxygen doping, and the peaks appearing at 280.5 cm^{-1} and 337.5 cm^{-1} showed that the MoS_2 lattice was contracted under the influence of oxygen doping. All these results fully demonstrated the successful doping of oxygen in the ultrathin MoS_2 nanosheets. In fact, in experiments, oxygen doping inevitably strains ultrathin MoS_2 nanosheets, and this strain also play an important role in enhancing the catalytic activity of the HER [40]. In order to more intuitively elucidate the effects of oxygen doping and strain on HER performance, the calculation of the free energy (ΔG_{H*}) of atomic hydrogen adsorption (Figure 6D) was used to show that the ΔG_{H*} of strained MoS_2 with oxygen doping was only 0.3 eV, which was much lower than that of pristine MoS_2. Based on the analysis of these experimental results, a schematic diagram of the formation mechanism of $MoS_{2-x}O_x$ during the reaction was established. As shown in Figure 6E, the introduction of O_2 induced the electron cloud rearrangement of the S 2p orbital, leading to the breakage of the Mo-S bond, the generation of volatile SO_2 species, and the production of S vacancies. Figure 6F shows a complete actual reaction mechanism diagram. Excitation by the light of EY was found to produce the triplet excited state EY^{3*} and the free radical EY^- through the reductive quenching of TEOA. Next the electrons were transferred between the highly reducible EY^- and O_2, the generated O^-_2 continued to react with MoS_2, and oxygen doping was finally achieved. With the formation of $MoS_{2-x}O_x$, the catalyst had a locally higher electron density and better electrical conductivity. In other words, oxygen doping and the strain brought by oxygen doping could optimize the electronic structure and Gibbs free energy of the catalyst and realize the phenomenon of the self-optimization of catalyst performance. These studies aid our understanding of the evolution of chemical components in in situ reconstruction phenomena and also provide new insights into the design of new catalyst studies.

2.4. Phase Transition Refactoring

Phase change is the process of the transformation of a substance from one phase to another. Extensive studies have shown that some catalysts inevitably undergo phase transition due to the presence of cathodic potential and strong adsorption–surface interactions during the HER. The atomic density, coordination number, strain density, and electronic structure of the catalyst surface also change [41,42]. Our group reported that the irreversible phase transition of MoS_2 during the photocatalytic HER resulted in a significant increase

in catalytic activity [20]. The photocatalytic HER of TiO_2@MoS_2 was carried out under visible light irradiation using Eosin Y (EY) as the photosensitizer and triethanolamine (TEOA) as the sacrificial agent, and the hydrogen yields were separately examined. The results showed (Figure 7A) that the hydrothermally exfoliated TiO_2@MoS_2 exhibited better HER activity than the pre-exfoliated TiO_2@MoS_2, and the highest catalytic activity of the hydrothermally exfoliated TiO_2@MoS_2 was reached after 7 h from the start of the reaction (Figure 7B). The HRTEM test results clearly showed the reason for the self-optimization performance (Figure 7C,D). The catalyst showed a distortion of the 1T′ phase, as the 1T phase gradually relaxed into a highly distorted 1T′ phase with a superlattice, and its superlattice structure also aggregated from Mo atoms into a jagged chain structure. To further elucidate the mechanism by which this phase transition occurs, it was investigated by calculating ΔG_H as a function of strain for different adsorption sites (Figure 7E,F) on different phases of MoS_2 (Figure 7G,H). The calculated results showed that even though certain active sites were present on both 1T and 1T′ basal planes, the 1T′ phase confirmed its high hydrogen precipitation activity performance with ΔG_H values of below 0.35 eV (regardless of the adsorption sites and the coverage of H), i.e., the self-optimization of the catalytic performance of MoS_2 was induced by it undergoing a transition from the 1T to the 1T′ phase.

Unlike the direct observation of phase transition phenomena in the experiments mentioned above, our group innovatively proposed the in situ reconstruction of WS_2 via local strain engineering and successfully transformed 2H-WS_2 nanoribbons into 1T-WS_2 nanospirals, and we found that it showed a high catalytic activity and good stability as a HER catalyst [43]. Due to the unique nanoribbon structure of 2H-WS_2 with a strain gradient prepared by a simple hydrothermal synthesis method, coupled with the more flexible thinner nanoribbons, 2H-WS_2 spontaneously twisted into a helix when subjected to anisotropic driving forces. In this process, the S-plane slipped due to the twisting of the atomic plane, but stable 1T-WS_2 nanospirals were eventually formed due to the Van der Waals interactions between the layers and the self-stabilizing energy of the helix [44,45]. Based on this theory, three atomic models were constructed, as shown in Figure 7I, to illustrate that mechanically stretching WS_2 nanoribbons into pleated sheets could be considered a typical way to induce shape anisotropy, thus making it possible to thermodynamically induce phase transitions by mechanical deformation [46–49]. Figure 7K clearly shows the formation energy difference $\Delta\gamma$ between the 2H phase and the 1T phase (Figure 7J) as a function of strain. Clearly, the 1T phase was more stable than the 2H phase when the strain was close to 5%. This reinforced the feasibility of the theory. Remarkably, the next performance test on the 1T-WS_2 nano helix in the HER showed good and efficient self-optimized catalytic activity, i.e., an overpotential of 170 mV at an electrocatalytic current density of 10 mA cm^{-2} (Figure 7L) and a Tafel slope of 40 mV dec^{-1} (Figure 7M), which implied the feasibility of the in situ reconstitution of WS_2 by local strain engineering pairs. In the SEM image of WS_2 that was subjected to 20,000 cycles (Figure 7N), it can be clearly seen that the WS_2 nano helices were interconnected and formed an open porous framework, which not only exposed more active edges [50–53] but also provided the inner surface of the 1T-WS_2 electrode with a larger contact area with the solution. Additionally, the results of the density generalization calculations of the atomic hydrogen adsorption free energy of deformed 1T-WS_2 monolayers at different strains showed (Figure 7O) that the edges of 1T-WS_2 had lower $\triangle G_H$ values than 2H-WS_2, indicating that both the electron transport efficiency and active sites were enhanced by the phase transition. Furthermore, Sun et al. studied the phase transition reconfiguration of multivalent nickel sulfides in the HER process and suggested that the phase reconfiguration process could be synergistically accelerated by moderate Fe doping to improve HER performance [54]. It was found that NiS_2 doped with 20% Fe had better catalytic performance than NiS_2 alone, and it was found that not only NiS_2 but also multivalent nickel sulfides such as α-NiS, β-NiS, and Ni_3S_4 had similar phase transition processes, as shown in Figure 7P,Q. This not only indicated that the phase reconfiguration of NiS_2 penetrated from the surface to the matrix over long catalytic

durations and thus enhanced the catalytic activity of the catalyst but also illustrated the prevalence of the phase reconfiguration of multivalent nickel sulfide catalysts in the HER process. Overall, the phase transformation tended to bring benefits such as a lower charge transfer resistance, enhanced activity per site, and an increased number of active sites due to topological phase transformation of the catalysts, as well as providing a new approach for designing new catalysts with self-optimized activity via in situ reconfiguration.
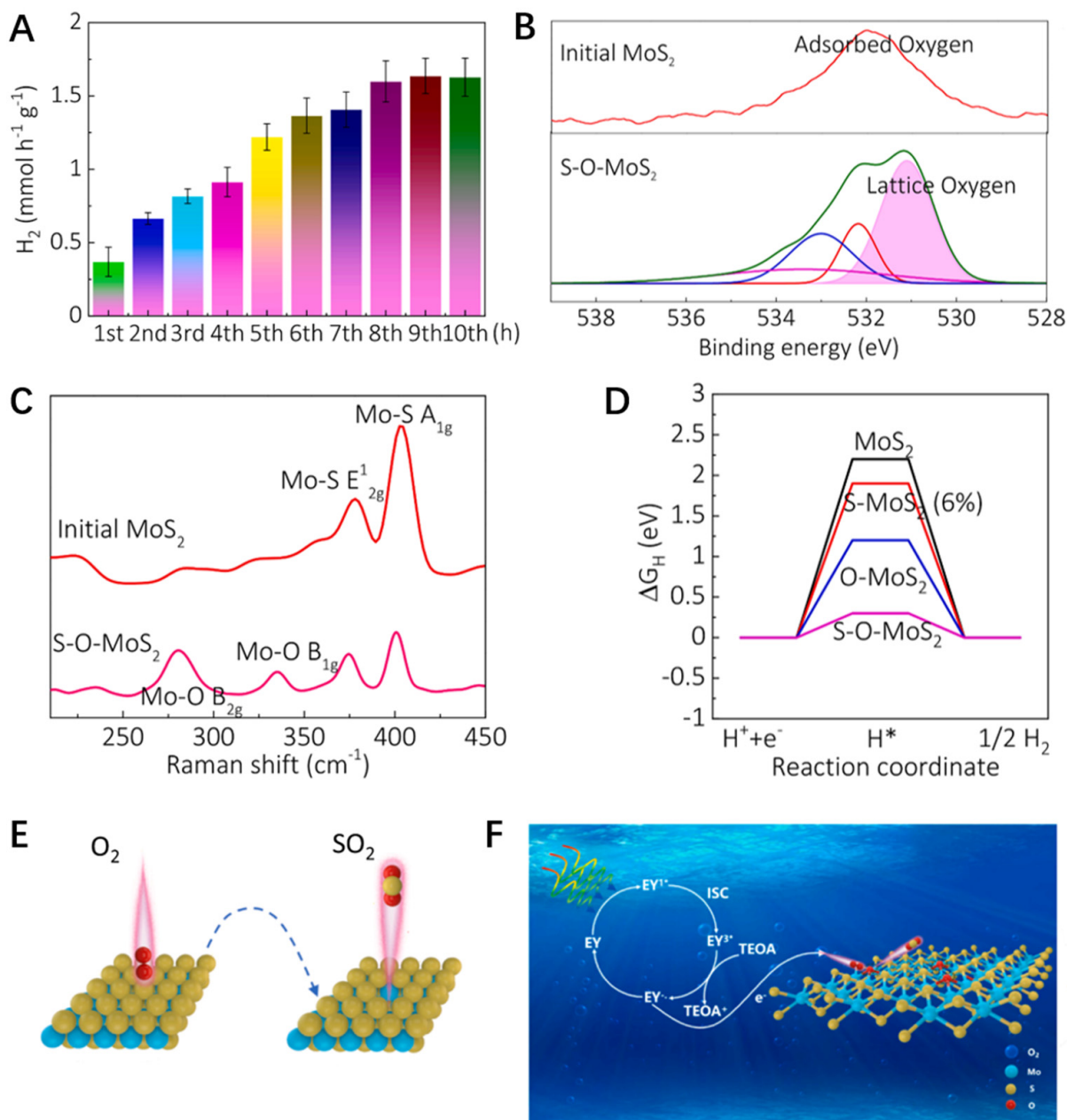
Figure 6. (**A**) Plot of the results of hydrogen production per hour of MoS_2 during the HER detected with an online gas chromatograph every 15 min. (**B**) O 1s high-resolution XPS spectra and (**C**) Raman spectra of pristine MoS_2 and S-O-MoS_2. (**D**) Hydrogen precipitation ΔG_{H*} plots of pristine MoS_2, strained MoS_2 (S-MoS_2, 6% strain), O-doped MoS_2 (O-MoS_2, 25 atom% O) and O-doped strained MoS_2 (S-O-MoS_2, 6% strain, 25 atom% O). (**E**) Schematic diagram of the S vacancy formation process. (**F**) Schematic diagram of the formation mechanism of $MoS_{2-x}O_x$ during the actual reaction. Reproduced with permission [2021], Copyright 2021, Elsevier.
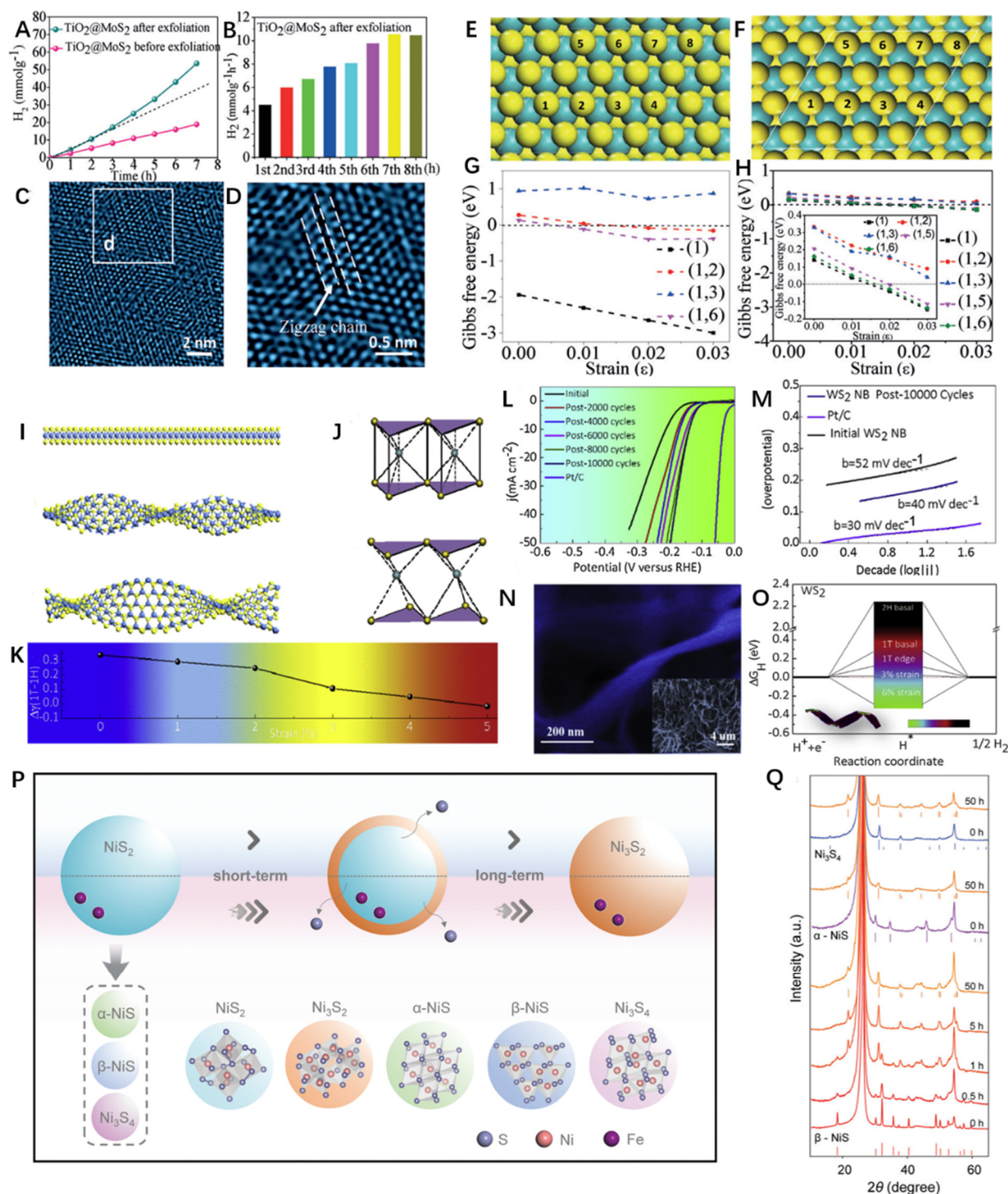
Figure 7. (**A**) H_2 accumulation and (**B**) H_2 production rate of TiO$_2$@MoS$_2$ over stripped TiO$_2$ during each hour of the HER. All experiments were performed in 80 mL of a 15% (*v/v*) TEOA aqueous solution under visible light irradiation (γ > 420 nm). (**C**) HRTEM images of MoS$_2$ in TiO$_2$@MoS$_2$ exfoliated after 7 h. (**D**) Magnified image of the square in (**C**) (arrows point to the serrated chain structure of 1T′). Supercell of H adsorbed on the surface of monolayer 1T-MoS$_2$ (**E**) and 1T′-MoS$_2$ (**F**). The yellow and blue balls indicate S and Mo atoms, respectively. The numbers indicate the possible sites of H binding. The Gibbs free energy for H adsorption on 1T-MoS$_2$ (**G**) and 1T′-MoS$_2$ (**H**) was calculated for strain (ε) in the range of 0.0% to 3.0%. (1) corresponds to 1/16 coverage of one H at any one site. (1,2), (1,3), (1,5) and (1,6) correspond to the coverage of two H atoms (one at 1 and the other at 2, 3, 5, and 6, respectively). 1T-MoS$_2$: (1,2) = (1,4); (1,3) = (1,5) = (1,7); (1,6) = (1,8). 1T′-MoS$_2$:

(1,2) = (1,4); (1,3) = (1,5) = (1,7); (1,6) = (1,8). 1T'-MoS$_2$: (1,2) = (1,4); (1,3) = (1,7); (1,6) = (1,8). Reproduced with permission [20], Copyright 2017, Wiley-VCH. (**I**) Strain-induced topological transition of WS$_2$ nanoribbons to nano helices. The yellow and blue spheres represent S and W atoms, respectively. Side views of the terminated armchair and twisted armchair WS$_2$ nanoribbons and helical WS$_2$ nanowires are shown from top to bottom. (**K**) The calculated formation energy difference $\Delta\gamma$ between the 2H and 1T (**J**) phases as a function of strain. (**L**) Electrochemical data of WS$_2$ nanoribbons with a Pt reference catalyst in H$_2$SO$_4$ (0.5 M). Polarization curves are shown as a function of the number of potential cycles. (**M**) Corresponding Tafel plots of WS$_2$ nanoribbons, Pt/C, and pristine WS$_2$ nanoribbons after 10,000 cycles. (**N**) SEM image of WS$_2$ nanospiral (after 20,000 cycles of WS$_2$ nanoribbon). (**O**) ΔG_H plots of different H adsorption sites and comparison of the effect of different sites and strains on HER properties in 1T and 2H-WS$_2$ phases. The inset is a TEM image of a WS$_2$ nano helix. Reproduced with permission [43], Copyright 2019, Elsevier. (**P**) Schematic diagram of the phase reconfiguration of multivalent nickel sulfide HER catalysts. (**Q**) XRD spectra of different catalysts after the instantaneous action of the HER at a constant current density of 10 mA cm^{-2}. Reproduced with permission from [54], ©The Royal Society of Chemistry 2014.

2.5. Surface Defects

In recent years, defects have drawn a lot of attention and research for their ability to enhance intrinsic activity, enrich active sites, and improve electrical conductivity. Inspired by the fact that defects can change the charge distribution on a catalyst surface and thus directly generate active sites on the inert substrate, Charlie Tsai and colleagues proposed and verified that the application of a sufficient reduction potential could induce sulfur vacancies in monolayer and multilayer MoS$_2$ to enhance its HER catalytic activity [55]. As shown in Figure 8A, the calculation of the surface free energy of a single atom showed that the surface on which sulfur vacancies were generated after the application of a potential (*) was more stable and had a higher capacity for hydrogen adsorption than the original substrate (*S). It also reflected that the generated sulfur vacancies were more inclined to bind to H$_2$ than to the removed H$_2$S gas. A further complete theory of sulfur vacancy generation was presented, as shown in Figure 8B, i.e., the desulfurization process at the applied potential was realized following the step of transferring two electrons and protons to the sulfur atoms in the basal plane. The free energy diagram of the corresponding steps below then proved the correctness of the proposed reaction process [56,57]. Next, the feasibility of the electrochemical activation strategy was verified with further experiments. The electrochemical processes of sulfur vacancy generation in monolayer and multilayer molybdenum disulfide under different electrode supports were tested, and optical and SEM images of the experimental samples were obtained (Figure 8C,D). The images showed that the samples exhibited significant morphological changes after the applied potential for both monolayer and multilayer MoS$_2$, which implied the successful introduction of defects. The current density test results in Figure 8E show that the catalytic activity of both monolayer and multilayer MoS$_2$ was enhanced after the electrochemical desulfurization process. That is, the sulfur vacancies created during the electrochemical reaction played a decisive role in the self-optimization of their HER activity. Finally, Figure 8F shows the TOF of each surface Mo atom of the sample (TOF$_{Mo}$) versus the applied potential and compares it with the TOF of other MoS$_x$ groups currently considered to be the most advanced. Various state-of-the-art MoS$_x$ catalysts from [58] are shown with non-bold labels. The light green area is the MoS$_2$ monomolecular layer from [59] that underwent Ar desulfurization. The red solid curve is the monolayer MoS$_2$ on the Au substrate after electrochemical desulfurization, and the blue solid curve is the multilayer MoS$_2$ on carbon foam substrate after electrochemical desulfurization without iR correction. The blue dashed curve refers to the electrochemically desulfurized multilayer molybdenum disulfide on a carbon foam substrate with iR correction. The experimental samples exhibited higher TOF values. It was noteworthy that the experimentally prepared MoS$_2$ samples containing S

vacancies were not structurally optimized. Additionally, this could provide a feasible way to prepare more active and low-cost HER catalysts.
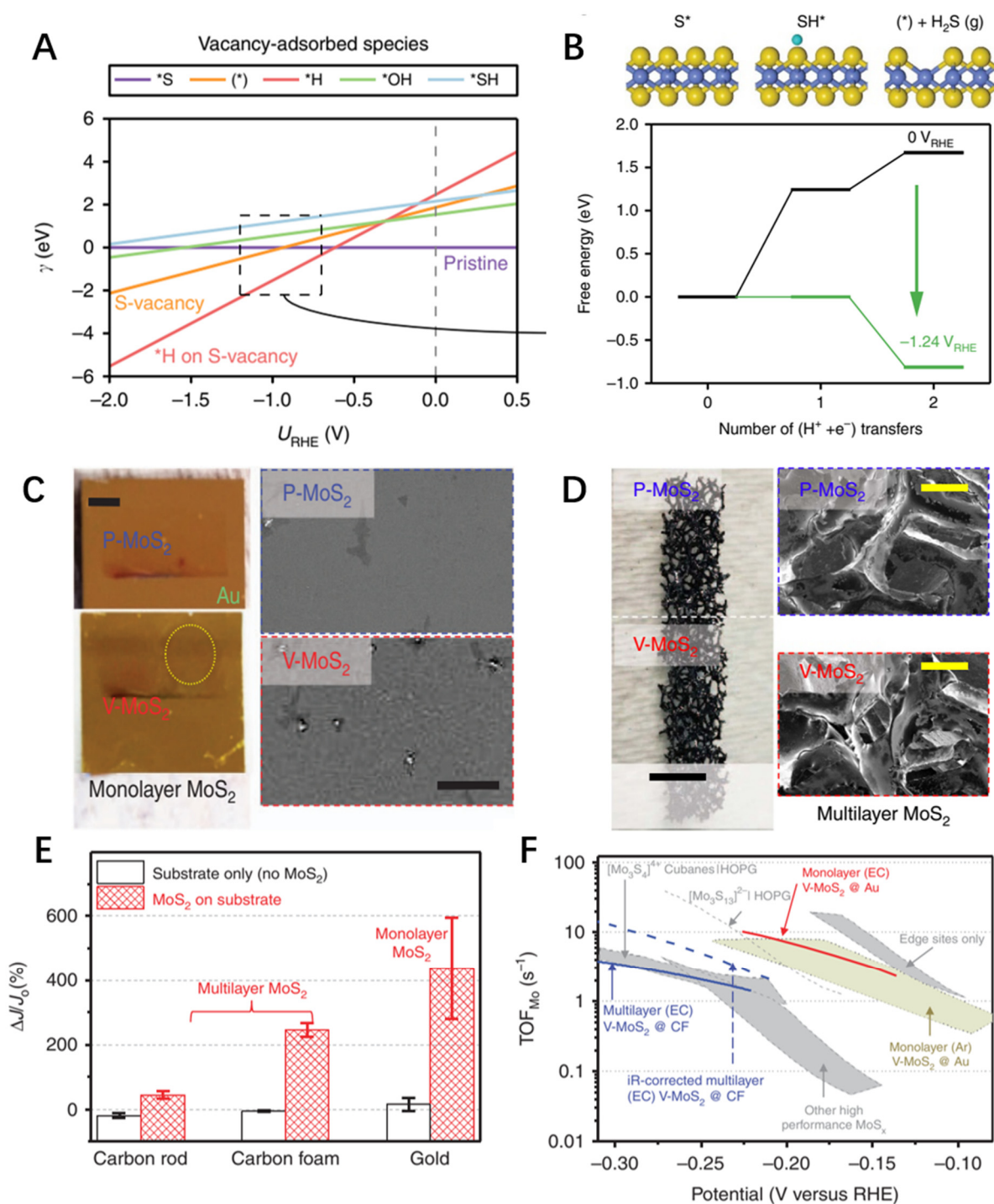
Figure 8. (**A**) The unit cell surface energy of 2H-MoS$_2$ at fixed sulfur vacancies as a function of the applied potential of 2H-MoS$_2$ substrates with different adsorbent species (3.1%). (*) refers to the S vacancy, and the adsorbed species in the S vacancy is indicated by the prefix *. For example, (*S) refers to the sulfur adsorbed in the vacancy, i.e., the original basal plane without the S vacancy. (**B**) A schematic diagram of the EC desulfurization process is shown at the top of the figure. The lower part shows the free energy diagram for the protonation and removal of S. The green line indicates the free energy path at the applied potential required to make all paths functional. (**C**) Optical and SEM images of monolayer MoS$_2$ before desulfurization (P-MoS$_2$) and after desulfurization (V-MoS$_2$).

(**D**) Optical and SEM images of multilayer MoS_2 films before (P-MoS_2) and after (V-MoS_2) desulfurization. (**E**) Statistics regarding the desulfurization effect of multilayer molybdenum disulfide on carbon rods and carbon foam substrates and the desulfurization effect of monolayer molybdenum disulfide on gold substrates on improving HER activity. The rods without MoS_2 attachment show negligible effects of the electrochemical desulfurization process on the substrate itself. Error bars indicate the standard deviation between samples. (**F**) Comparison of the TOF_{Mo} flip frequency of Mo atoms per surface between experimental samples and state-of-the-art MoS_x electrocatalysts. Reproduced with permission [55], Copyright 2017, Springer Nature.

2.6. Interface Refactoring

Recently, the ability of a pre-catalyst designed based on interfacially induced self-assembly to achieve efficient performance self-optimization through interfacial reconfiguration during the HER was demonstrated by Wang and colleagues [60]. A CoC_2O_4@MXene pre-catalyst with hollow nanotubes was synthesized by completing the self-assembly of CoC_2O_4 nanorods and MXene nanosheets in an aqueous oxalic acid dihydrate solution at room temperature under the influence of interfacially induced effects. Next, sequential LSV scans were performed in 1 M KOH. The results showed (Figure 9A) that CoC_2O_4@MXene had a stable polarization profile after only five scanning cycles, and the overpotential sharply dropped by about 46 mV during this process, ending up with an overpotential of only 28 mV at 10 mA cm^{-2} (Figure 9B). This indicated that CoC_2O_4@MXene could complete a fast, efficient reconstitution in a short period of time, making its own performance substantially improved. Further HRTEM (high-resolution transmission electron microscopy) showed (Figure 9C) that CoC_2O_4@MXene generated new hexagonal nanosheets after cycling. The observed 0.276 nm lattice stripe length was consistent with the (100) plane of $Co(OH)_2$, revealing that the formation of this sparse hexagonal nanosheet structure could be attributed to the generation of $Co(OH)_2$. The interfacial reconfiguration mechanism of the conversion of CoC_2O_4@MXene to $Co(OH)_2$ was proposed based on the experimental data, as shown in Figure 9D. Due to the ultrathin MXene and its unique nanotube structure, the high electron accessibility and abundant electrolyte diffusion channels introduced a highly disordered and sparse $Co(OH)_2$ nanosheet structure for the catalyst as the reaction process proceeded, forming a $Co(OH)_2$@MXene complex with low valence and rich defect levels. Finally, the catalytic mechanism of CoC_2O_4@MXene in the basic HER process after the interfacial reconfiguration is elucidated in the figure. As shown in Figure 9E,F, due to the low valence state and defect-rich nature of the complex formed by the rapid reconstruction, a large number of Co active sites were fully exposed, which promoted the adsorption of water molecules and optimized the binding energy of H* intermediates, thus accelerating the HER kinetics. Moreover, the large number of exposed low-valent Co sites also provided good orbitals for charge transfer, which consequently enhanced the electrical conductivity. In addition, the reconfigured $Co(OH)_2$@MXene complex still had good hydrophilicity, excellent conductivity and abundant electrolyte diffusion channels due to the sparse structure and ultrathin MXene of the in situ reconfigured catalyst. Therefore, interface refactoring often causes changes in the surface structure, active site, and conductivity of catalysts (e.g., the surface structure becomes loose and amorphous, the number or types of active sites increases, and the conductivity is optimized) so as to realize the self-optimization of catalyst performance from different angles and directions.
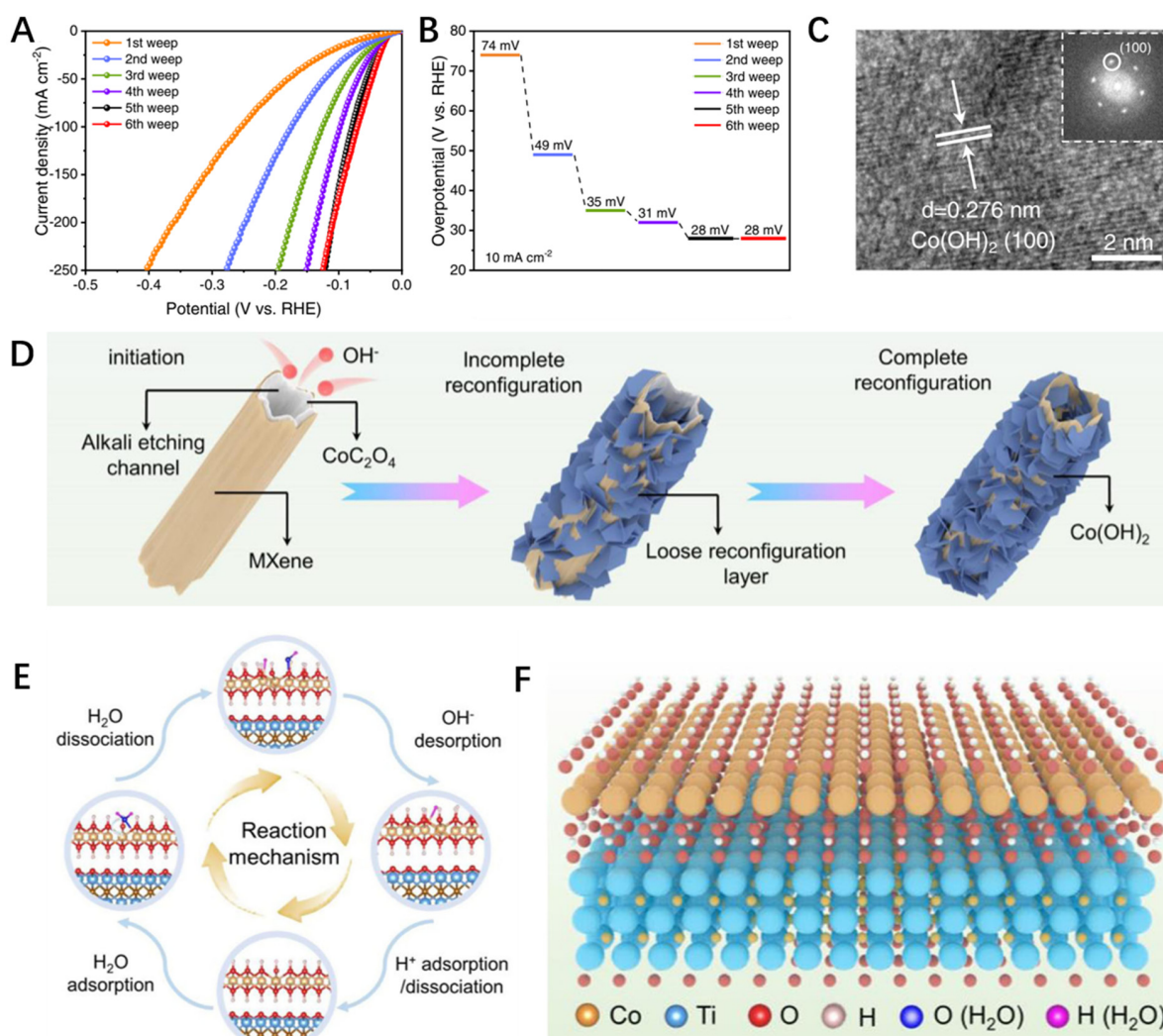
Figure 9. (**A**) Polarization curves of different LSV scans (IR correction) and (**B**) corresponding overpotentials of CoC$_2$O$_4$@MXene in a 1 M KOH solution. (**C**) HRTEM image of CoC$_2$O$_4$@MXene after the cycle. (**D**) Schematic diagram of the reconfiguration process of CoC$_2$O$_4$@MXene. (**E,F**) Schematic illustration of the catalytic mechanism of the alkaline HER on the CoC$_2$O$_4$@MXene after the cycle. Reproduced with permission from [60], ©Springer Nature 2017.

3. Synergistic Effects

A synergistic effect, a common phenomenon in society and scientific research, refers to the addition or blending of two or more components together, resulting in an effect greater than the sum of the various components acting individually [61]. With the rapid development of in situ characterization techniques in recent years, it has been found that the in situ reconfiguration of the surface of a portion of HER catalysts is often accompanied by a series of more fantastic chain evolutions, which consequently act on the catalytic performance of the catalysts and result in a greater enhancement of their catalytic activity [62]. Therefore, appropriate or controlled synergistic effects can be used as a more efficient and cost-effective catalyst activation strategy to achieve the self-optimization of catalyst performance. As mentioned above in the work of Qiu and colleagues, the high catalytic activity of the H-NiFe LDH is influenced not only by its better electron transfer rate due to its increased crystallinity but also by the enhanced performance of the catalyst combined with the adsorbate that forms intermediates that accelerate the rate of hydrolysis [18]. The efficiency of the synergistic effect was also very well-demonstrated in the work of Zou and colleagues mentioned above. It was found that the newly generated Fe@FeO$_x$S$_y$ nanoparticles were

not in the free state but were directly immobilized on FeS nanosheets [19]. We know that polymer binders are necessary for powdered catalysts [63,64]. The direct immobilization of the nanoparticles on the nanosheets in this kind of experiment not only eliminates the need for polymer binders and thus reduces the experimental cost and operational difficulties but also reduces the interfacial resistance between them and thus improves the electrode structure and catalytic stability. From these two examples, we can draw certain conclusions. Firstly, the synergistic effect can not only improve the performance of catalysts but also save time and economic costs to a certain extent. Secondly, since the synergistic effect is often a series of chain effects caused by one evolution, and such subtle effects are not easily observed, we must treat each experimental phenomenon and all data with a rigorous and careful attitude in the experimental process, which is essential to promote the development of science and technology. Table 1 shows the catalytic performance of electrocatalysts modulated via in situ surface reconstruction. It can be seen that in situ surface reconstruction is an important strategy for regulating catalytic hydrogen evolution.

Table 1. Catalytic performance of electrocatalysts modulated via in situ surface reconstruction.

Catalyst	Reconstruction Types	Electrolyte	Performance
H-NiFe LDH [18]	Reconfiguration of crystallinity	1.0 M KOH	Tafel slope of 62.30 mV dec^{-1}
H-TaS$_2$ [30]	Morphological evolution	0.5 M H$_2$SO$_4$	Tafel slope of 37 mV dec^{-1}
Fe@FeOxSy [19]	Complete species transition	1 M KOH	Tafel slope of 77 mV dec^{-1}
HxZIS [36]	In situ surface hydrogenation	0.35 M/0.25 M Na$_2$S-Na$_2$SO$_3$	90 µmol of H$_2$ at each hour of the HER
S-O-MoS$_2$ [37]	In situ surface oxygen doping	With O doping (20.0 mg) and 20 mg of EY dye in 100 mL of aqueous TEOA solution (15%, v/v) at pH 7	The maximum rate of H$_2$ production reached 1.6 mmol h^{-1} g^{-1}
TiO2@MoS$_2$ [20]	Phase transition refactoring	80 mL of 15% (v/v) aqueous TEOA solution under visible light irradiation (l > 420 nm); catalysts: 20 mg; EY: 20 mg	The maximum rate of H$_2$ production reached 10.5 mmol h^{-1} g^{-1}
1T-WS$_2$ [43]	Phase transition refactoring	0.5 M H$_2$SO$_4$	Tafel slope of 40 mV dec^{-1}
Multilayer MoS$_2$ [55]	Surface defects	0.5 M H$_2$SO$_4$	Tafel slope of 102 mV dec^{-1}
Monolayer MoS$_2$ [55]	Surface defects	0.5 M H$_2$SO$_4$	TOF = 1.0 s^{-1} at −100 mV
Co(OH)$_2$@MXene [60]	Interface refactoring	1 M KOH	A low overpotential of 28 mV at 10 mA cm^{-2}

4. Conclusions and Future Prospects

Despite many practical achievements in transition metal catalyst design and performance enhancement, research on issues such as the understanding of in situ reconstructions and performance self-optimization is still in an immature stage. In this work, we reviewed the in situ surface reconstruction of catalysts during the HER process, focusing on six aspects of crystallinity change, morphology evolution, chemical component evolution, phase transition, surface defects, and interface refactoring, and we established the link between structure and performance. Overall, it is clear from our summary and analysis that in situ reconstructions have significant effects on the performance of catalysts in chemical reactions. Therefore, a more in-depth study on the in situ reconstruction of catalysts to reveal and summarize the potential mechanisms and principles is important to produce the next generation of catalysts with low cost, high activity, high selectivity, and long-term stability, as well as to further promote the commercialization of hydrogen energy production to achieve the goal of sustainable development [14,65]. However, the realistic feasibility of these in situ reconstructions remains to be explored in depth, so we suggest that future work should pay attention to the following ideas.

Firstly, in situ surface reconstruction is being continuously enriched, which can systematically reveal the predicted in situ surface reconstruction phenomena of HER catalysts. At present, the dynamic evolution of HER catalysts during the reaction process has not received sufficient attention and in-depth study, and more attention has been paid to CO_2RR (carbon dioxide reduction reaction) [66–70], NRR (nitrogen reduction reaction) [71–74], and OER (oxygen evolution reaction) [75–79]. In addition, theoretical calculations, an indispensable tool for experimental characterization, have mostly been used to analyze the effects of these dynamics and have not been skillfully applied to analyze and predict changes in the catalysts themselves. Therefore, it is important to establish a mature knowledge system of the in situ surface reconstruction of HER catalysts and to analyze and predict the dynamic change process of catalysts with the help of theoretical calculations for the design of high-performance, high-stability and high-selectivity HER catalysts.

Secondly, a multifaceted and complementary in situ characterization technology system has been established in order to more comprehensively and deeply track the dynamic evolution of HER catalysts in the catalytic process and to identify and capture the true intrinsic active sites of catalysts in a timely and accurate manner. With the advancement of technology, more and more in situ characterization techniques, such as XPS, XRD, Raman spectroscopy and SECM, have been used as experimental characterization tools for HER catalysts [15,65]. However, it is worth noting that each of these technical tools has the characteristics of harsh application conditions and narrow application targets [38,80–82]. Therefore, it is difficult to achieve a comprehensive and profound understanding of the in situ surface reconstruction of HER catalysts with a single technical characterization tool [83–89]. Therefore, in future experimental studies, a combination of techniques with various temporal resolutions and probing regions (e.g., contact interfaces, solids, and liquids) should be adopted to characterize the in situ surface reconstruction phenomena in a comprehensive manner.

In addition, more groundbreaking methods should be developed, such as the integration of existing in situ reconstruction examples by means of the statistical analysis of big data and artificial intelligence algorithms, in order to build and analyze all possible in situ reconstruction models [81,90–93]. Big data and artificial intelligence technologies are both hot research fields nowadays, and they have seen widespread attention and rapid development due to their time-saving and efficient nature. With the involvement of artificial intelligence and machine learning, theoretical simulations may be able to provide a clear description of structural evolutions and reactive pathways [70,82], which will consequently guide researchers in deeper exploration and discovery.

Author Contributions: Writing—review and editing, Y.Z., J.P., G.G., R.S., Y.Y., M.L.; W.H., P.F. and L.Y., project administration, L.W.; All authors have read and agreed to the published version of the manuscript.

Funding: This work was financially supported by the Natural Science Foundation of China (51902101), the Youth Natural Science Foundation of Hunan Province (2021JJ540044), the Natural Science Foundation of Jiangsu Province (BK20201381), and the Science Foundation of Nanjing University of Posts and Telecommunications (NY219144).

Conflicts of Interest: The authors declare that they have no known competing financial interests or personal relationships that could have appeared to influence the work reported in this paper.

References

1. Fang, Y.; Fang, Y.; Zong, R.; Yu, Z.; Tao, Y.; Shao, J. In situ surface reconstruction of a Ni-based perovskite hydroxide catalyst for an efficient oxygen evolution reaction. *J. Mater. Chem. A* **2022**, *10*, 1369–1379. [CrossRef]
2. Polo-Garzon, F.; Bao, Z.; Zhang, X.; Huang, W.; Wu, Z. Surface Reconstructions of Metal Oxides and the Consequences on Catalytic Chemistry. *ACS Catal.* **2019**, *9*, 5692–5707. [CrossRef]
3. Zhang, A.; Liang, Y.; Li, H.; Zhang, B.; Liu, Z.; Chang, Q.; Zhang, H.; Zhu, C.-F.; Geng, Z.; Zhu, W.; et al. In-Situ Surface Reconstruction of InN Nanosheets for Efficient CO_2 Electroreduction into Formate. *Nano Lett.* **2020**, *20*, 8229–8235. [CrossRef] [PubMed]

4. Pi, Y.; Xu, Y.; Li, L.; Sun, T.; Huang, B.; Bu, L.; Ma, Y.; Hu, Z.; Pao, C.-W.; Huang, X. Selective Surface Reconstruction of a Defective Iridium-Based Catalyst for High-Efficiency Water Splitting. *Adv. Mater.* **2020**, *30*, 2004375. [CrossRef]

5. Cao, D.; Sheng, B.; Qi, Z.; Xu, W.; Chen, S.; Moses, O.; Long, R.; Xiong, Y.; Wu, X.; Song, L. Self-optimizing iron phosphorus oxide for stable hydrogen evolution at high current. *Appl. Catal. B* **2021**, *298*, 120559. [CrossRef]

6. Ryu, J.; Jung, N.; Jang, J.; Kim, H.-J.; Yoo, S. In Situ Transformation of Hydrogen-Evolving CoP Nanoparticles: Toward Efficient Oxygen Evolution Catalysts Bearing Dispersed Morphologies with Co-oxo/hydroxo Molecular Units. *ACS Catal.* **2015**, *5*, 4066–4074. [CrossRef]

7. Luo, Y.; Tang, L.; Khan, U.; Yu, Q.; Cheng, H.-M.; Zou, X.; Liu, B. Morphology and surface chemistry engineering toward pH-universal catalysts for hydrogen evolution at high current density. *Nat. Commun.* **2019**, *10*, 269. [CrossRef]

8. Wei, M.; Yang, L.; Wang, L.; Liu, T.; Liu, C.; Tang, Y.; Luo, S. In-situ potentiostatic activation to optimize electrodeposited cobalt-phosphide electrocatalyst for highly efficient hydrogen evolution in alkaline media. *Chem. Phys. Lett.* **2017**, *681*, 90–94. [CrossRef]

9. Shao, Z.; Zhu, Q.; Sun, Y.; Zhang, Y.; Jiang, Y.; Deng, S.; Zhang, W.; Huang, K.; Feng, S. Phase-Reconfiguration-Induced $NiS/NiFe_2O_4$ Composite for Performance-Enhanced Zinc−Air Batteries. *Adv. Mater.* **2022**, *34*, 2110172. [CrossRef]

10. Xie, C.; Chen, W.; Du, S.; Yan, D.; Zhang, Y.; Chen, J.; Liu, B.; Wang, S. In-situ phase transition of WO_3 boosting electron and hydrogen transfer for enhancing hydrogen evolution on Pt. *Nano Energy* **2020**, *71*, 104653. [CrossRef]

11. Ozden, S.; Bawari, S.; Vinod, S.; Martinez, U.; Susarla, S.; Narvaez, C.; Joyner, J.; Tiwary, C.; Narayanan, T.; Ajayan, P. Interface and defect engineering of hybrid nanostructures toward an efficient HER catalyst. *Nanoscale* **2019**, *11*, 12489–12496. [CrossRef] [PubMed]

12. Xie, J.; Qu, H.; Xin, J.; Zhang, X.; Cui, G.; Zhang, X.; Bao, J.; Tang, B.; Xie, Y. Defect-rich MoS_2 nanowall catalyst for efficient hydrogen evolution reaction. *Nano Res.* **2017**, *10*, 1178–1188. [CrossRef]

13. Shi, R.; Shang, L.; Zhou, C.; Zhao, Y.; Zhang, T. Interfacial wettability and mass transfer characterizations for gas–liquid–solid triple-phase catalysis. *Exploration* **2022**, *2*, 20210046. [CrossRef]

14. Zhang, W.; Yang, Y.; Tang, Y.; Gao, Q. In-situ reconstruction of catalysts in cathodic electrocatalysis: New insights into active-site structures and working mechanisms. *J. Energy Chem.* **2022**, *70*, 414–436. [CrossRef]

15. Long, C.; Han, J.; Guo, J.; Yang, C.; Liu, S.; Tang, Z. Operando toolbox for heterogeneous interface in electrocatalysis. *Chem. Catal.* **2021**, *1*, 509–522. [CrossRef]

16. Li, X.; Yang, X.; Zhang, J.; Huang, Y.; Liu, B. In Situ/Operando Techniques for Characterization of Single-Atom Catalysts. *ACS Catal.* **2019**, *9*, 2521–2531. [CrossRef]

17. Li, X.; Wang, H.-Y.; Yang, H.; Cai, W.; Liu, S.; Liu, B. In Situ/Operando Characterization Techniques to Probe the Electrochemical Reactions for Energy Conversion. *Small Methods* **2018**, *2*, 1700395. [CrossRef]

18. Qiu, Z.; Tai, C.-W.; Niklasson, G.; Edvinsson, T. Direct observation of active catalyst surface phases and the effect of dynamic self-optimization in NiFe-layered double hydroxides for alkaline water splitting. *Energy Environ. Sci.* **2019**, *12*, 572–581. [CrossRef]

19. Zou, X.; Wu, Y.; Liu, Y.; Liu, D.; Li, W.; Gu, L.; Liu, H.; Wang, P.; Sun, L.; Zhang, Y. In Situ Generation of Bifunctional, Efficient Fe-Based Catalysts from Mackinawite Iron Sulfide for Water Splitting. *Chemistry* **2018**, *4*, 1139–1152. [CrossRef]

20. Wang, L.; Liu, X.; Luo, J.; Duan, X.; Crittenden, J.; Liu, C.; Zhang, S.; Pei, Y.; Zeng, Y.; Duan, X. Self-Optimization of the Active Site of Molybdenum Disulfide by an Irreversible Phase Transition during Photocatalytic Hydrogen Evolution. *Angew. Chem. Int. Ed.* **2017**, *56*, 7610–7614. [CrossRef]

21. Gao, Q.; Zhang, W.; Shi, Z.; Yang, L.; Tang, Y. Structural Design and Electronic Modulation of Transition-Metal-Carbide Electrocatalysts toward Efficient Hydrogen Evolution. *Adv. Mater.* **2019**, *31*, 1802880. [CrossRef] [PubMed]

22. Jin, H.; Guo, C.; Liu, X.; Liu, J.; Vasileff, A.; Jiao, Y.; Zheng, Y.; Qiao, S.-Z. Emerging Two-Dimensional Nanomaterials for Electrocatalysis. *Chem. Rev.* **2018**, *118*, 6337–6408. [CrossRef] [PubMed]

23. Shi, Y.; Zhang, B. Recent advances in transition metal phosphide nanomaterials: Synthesis and applications in hydrogen evolution reaction. *Chem. Soc. Rev.* **2016**, *45*, 1529–1541. [CrossRef] [PubMed]

24. Zhao, H.; Yuan, Z.-Y. Surface/interface engineering of high-efficiency noble metal-free electrocatalysts for energy-related electrochemical reactions. *J. Energy Chem.* **2021**, *54*, 89–104. [CrossRef]

25. Wang, W.; Wang, Z.; Yang, R.; Duan, J.; Liu, Y.; Nie, A.; Li, H.; Xia, B.; Zhai, T. In Situ Phase Separation into Coupled Interfaces for Promoting CO_2 Electroreduction to Formate over a Wide Potential Window. *Angew. Chem. Int. Ed.* **2021**, *60*, 22940–22947. [CrossRef]

26. Dutta, A.; Kuzume, A.; Rahaman, M.; Vesztergom, S.; Broekmann, P. Monitoring the Chemical State of Catalysts for CO_2 Electroreduction: An In Operando Study. *ACS Catal.* **2015**, *5*, 7498–7502. [CrossRef]

27. Zhao, D.; Zhang, R.; Dai, M.; Liu, H.; Jian, W.; Bai, F.-Q.; Wu, X. Constructing High Efficiency $CoZn_xMn_{2-x}O_4$ Electrocatalyst by Regulating the Electronic Structure and Surface Reconstruction. *Small* **2022**, *18*, 2107268. [CrossRef]

28. Klaus, S.; Cai, Y.; Louie, M.; Trotochaud, L.; Bell, A. Effects of Fe Electrolyte Impurities on $Ni(OH)_2/NiOOH$ Structure and Oxygen Evolution Activity. *J. Phys. Chem. C* **2015**, *119*, 7243–7254. [CrossRef]

29. Trotochaud, L.; Young, S.; Ranney, J.; Boettcher, S. Nickel–Iron Oxyhydroxide Oxygen-Evolution Electrocatalysts: The Role of Intentional and Incidental Iron Incorporation. *J. Am. Chem. Soc.* **2014**, *136*, 6744–6753. [CrossRef]

30. Liu, Y.; Wu, J.; Hackenberg, K.; Zhang, J.; Wang, Y.; Yang, Y.; Keyshar, K.; Gu, J.; Ogitsu, T.; Vajtai, R.; et al. Self-optimizing, highly surface-active layered metal dichalcogenide catalysts for hydrogen evolution. *Nat. Energy* **2017**, *2*, 17127. [CrossRef]

31. Iqbal, S.; Pan, Z.; Zhou, K. Enhanced photocatalytic hydrogen evolution from in situ formation of few-layered MoS_2/CdS nanosheet-based van der Waals heterostructures. *Nanoscale* **2017**, *9*, 6638–6642. [CrossRef] [PubMed]

32. Reddy, D.; Choi, J.; Lee, S.; Kim, Y.; Hong, S.; Kumar, D.; Kim, T. Hierarchical dandelion-flower-like cobalt-phosphide modified CdS/reduced graphene oxide-MoS_2 nanocomposites as a noble-metal-free catalyst for efficient hydrogen evolution from water. *Catal. Sci. Technol.* **2016**, *6*, 6197–6206. [CrossRef]

33. Han, B.; Liu, S.; Zhang, N.; Xu, Y.-J.; Tang, Z.-R. One-dimensional CdS@MoS_2 core-shell nanowires for boosted photocatalytic hydrogen evolution under visible light. *Appl. Catal. B Environ.* **2017**, *202*, 298–304. [CrossRef]

34. Mu, Y.; Jia, F.; Ai, Z.; Zhang, L. Iron oxide shell mediated environmental remediation properties of nano zero-valent iron. *Environ. Sci. Nano.* **2017**, *4*, 27–45. [CrossRef]

35. Jiang, D.; Yang, L.; Yuan, H.; Zhao, L.; Yu, J.; Liu, X.; Wang, Y.; Zhang, T.; Dong, T.; Huang, M.; et al. Saturated hydrogen regulated ti coordination of metallic TiH_2/Ti electrode via in-situ electrochemical hydrogenation for enhanced hydrogen evolution reaction. *Nano Energy.* **2022**, *93*, 106892. [CrossRef]

36. Zhu, Y.; Wang, L.; Liu, Y.; Shao, L.; Xia, X. In-situ hydrogenation engineering of $ZnIn_2S_4$ for promoted visible-light water splitting. *Appl. Catal. B Environ.* **2019**, *241*, 483–490. [CrossRef]

37. Wang, L.; Xie, L.; Zhao, W.; Liu, S.; Zhao, Q. Oxygen-facilitated dynamic active-site generation on strained MoS_2 during photo-catalytic hydrogen evolution. *Chem. Eng. J.* **2021**, *405*, 127028. [CrossRef]

38. Jones, R.; Hooper, D.; Zhang, L.; Wolverson, D.; Valev, V. Raman Techniques: Fundamentals and Frontiers. *Nanoscale Res. Lett.* **2019**, *14*, 231. [CrossRef]

39. Guo, S.; Li, Y.; Tang, S.; Zhang, Y.; Li, X.; Sobrido, A.; Titirici, M.-M.; Wei, B. Monitoring Hydrogen Evolution Reaction Intermediates of Transition Metal Dichalcogenides via Operando Raman Spectroscopy. *Adv. Funct. Mater.* **2020**, *30*, 2003035. [CrossRef]

40. Yu, L.; Ruzsinszky, A.; Perdew, J. Bending Two-Dimensional Materials to Control Charge Localization and Fermi-Level Shift. *Nano Lett.* **2016**, *16*, 2444–2449. [CrossRef]

41. Güller, F.; Llois, A.; Goniakowski, J.; Noguera, C. Prediction of structural and metal-to-semiconductor phase transitions in nanoscale MoS_2, WS_2, and other transition metal dichalcogenide zigzag ribbons. *Phys. Rev. B* **2015**, *91*, 075407. [CrossRef]

42. Calandra, M. Chemically exfoliated single-layer MoS_2: Stability, lattice dynamics, and catalytic adsorption from first principles. *Phys. Rev. B* **2013**, *88*, 245428. [CrossRef]

43. Wang, L.; Zhou, G.; Luo, H.; Zhang, Q.; Wang, J.; Zhao, C.; Rao, A.; Xu, B.; Lu, B. Enhancing catalytic activity of tungsten disulfide through topology. *Appl. Catal. B Environ.* **2019**, *256*, 117802. [CrossRef]

44. Yang, M.; Kotov, N. Nanoscale helices from inorganic materials. *J. Mater. Chem.* **2011**, *21*, 6775–6792. [CrossRef]

45. Deepak, F.; Esparza, R.; Borges, B.; López-Lozano, X.; Jose-Yacaman, M. Rippled and Helical MoS_2 Nanowire Catalysts: An Aberration Corrected STEM Study. *Catal. Lett.* **2011**, *141*, 518–524. [CrossRef]

46. Liu, Q.; Li, X.; Xiao, Z.; Zhou, Y.; Chen, H.; Khalil, A.; Xiang, T.; Xu, J.; Chu, W.; Wu, X.; et al. Stable Metallic 1T-WS_2 Nanoribbons Intercalated with Ammonia Ions: The Correlation between Structure and Electrical/Optical Properties. *Adv. Mater.* **2015**, *27*, 4837–4844. [CrossRef]

47. Li, S.; Lin, Y.-C.; Zhao, W.; Wu, J.; Wang, Z.; Hu, Z.; Shen, Y.; Tang, D.-M.; Wang, J.; Zhang, Q.; et al. Vapour–liquid–solid growth of monolayer MoS_2 nanoribbons. *Nat. Mater.* **2018**, *17*, 535–542. [CrossRef] [PubMed]

48. Luo, J.; Liu, T.; Zhang, D.; Yin, K.; Wang, D.; Zhang, W.; Liu, C.; Yang, C.; Wei, Y.; Wang, L.; et al. The individual and Co-exposure degradation of benzophenone derivatives by UV/H_2O_2 and UV/PDS in different water matrices. *Water Res.* **2019**, *159*, 102–110. [CrossRef] [PubMed]

49. Tian, Z.; Huang, W.; Xu, B.; Li, X.; Mei, Y. Anisotropic Rolling and Controlled Chirality of Nanocrystalline Diamond Nanomembranes toward Biomimetic Helical Frameworks. *Nano Lett.* **2018**, *18*, 3688–3694. [CrossRef]

50. Li, X.; Wu, M.; Xu, B.; Liu, R.; Ouyang, C. Compressive strain induced dynamical stability of monolayer 1T-MX_2 (M=Mo, W.; X=S, Se). *Mater. Res. Express.* **2017**, *4*, 115018. [CrossRef]

51. Cheng, W.; Zhao, X.; Su, H.; Tang, F.; Che, W.; Zhang, H.; Liu, Q. Lattice-strained metal–organic-framework arrays for bifunctional oxygen electrocatalysis. *Nat. Energy* **2019**, *4*, 115–122. [CrossRef]

52. Wang, H.; Xu, S.; Tsai, C.; Li, Y.; Liu, C.; Zhao, J.; Liu, Y.; Yuan, H.; Abild-Pedersen, F.; Prinz, F.; et al. Direct and continuous strain control of catalysts with tunable battery electrode materials. *Science* **2016**, *354*, 1031–1036. [CrossRef] [PubMed]

53. Johari, P.; Shenoy, V. Tuning the Electronic Properties of Semiconducting Transition Metal Dichalcogenides by Applying Mechanical Strains. *ACS Nano* **2012**, *6*, 5449–5456. [CrossRef] [PubMed]

54. Sun, Y.; Wu, J.; Zhang, Z.; Liao, Q.; Zhang, S.; Wang, X.; Xie, Y.; Ma, K.; Kang, Z.; Zhang, Y. Phase reconfiguration of multivalent nickel sulfides in hydrogen evolution. *Energy Environ. Sci.* **2022**, *15*, 633–644. [CrossRef]

55. Tsai, C.; Li, H.; Park, S.; Park, J.; Han, H.; Nørskov, J.; Zheng, X.; Abild-Pedersen, F. Electrochemical generation of sulfur vacancies in the basal plane of MoS_2 for hydrogen evolution. *Nat. Commun.* **2017**, *8*, 15113. [CrossRef]

56. Peterson, A.; Abild-Pedersen, F.; Studt, F.; Rossmeisl, J.; Nørskov, J. How copper catalyzes the electroreduction of carbon dioxide into hydrocarbon fuels. *Energy Environ. Sci.* **2010**, *3*, 1311–1315. [CrossRef]

57. Nørskov, J.; Rossmeisl, J.; Logadottir, A.; Lindqvist, L.; Kitchin, J.; Bligaard, T.; Jónsson, H. Origin of the Overpotential for Oxygen Reduction at a Fuel-Cell Cathode. *J. Phys. Chem. B* **2004**, *108*, 17886–17892. [CrossRef]

58. Benck, J.; Hellstern, T.; Kibsgaard, J.; Chakthranont, P.; Jaramillo, T. Catalyzing the Hydrogen Evolution Reaction (HER) with Molybdenum Sulfide Nanomaterials. *ACS Catal.* **2014**, *4*, 3957–3971. [CrossRef]

59. Li, H.; Tsai, C.; Koh, A.; Cai, L.; Contryman, A.; Fragapane, A.; Zhao, J.; Han, H.; Manoharan, H.; Abild-Pedersen, F.; et al. Activating and optimizing MoS_2 basal planes for hydrogen evolution through the formation of strained sulphur vacancies. *Nat. Mater.* **2016**, *15*, 48–53. [CrossRef]

60. Wang, L.; Hao, Y.; Deng, L.; Hu, F.; Zhao, S.; Li, L.; Peng, S. Rapid complete reconfiguration induced actual active species for industrial hydrogen evolution reaction. *Nat. Commun.* **2022**, *13*, 5785. [CrossRef]

61. Ying, Y.; Luo, X.; Qiao, J.; Huang, H. "More is Different:" Synergistic Effect and Structural Engineering in Double-Atom Catalysts. *Adv. Funct. Mater.* **2021**, *31*, 2007423. [CrossRef]

62. Abbas, S.; Kim, S.-H.; Iqbal, M.; Muhammad, S.; Yoon, W.-S.; Jung, K.-D. Synergistic effect of nano-Pt and Ni spine for HER in alkaline solution: Hydrogen spillover from nano-Pt to Ni spine. *Sci. Rep.* **2018**, *8*, 2986. [CrossRef] [PubMed]

63. Li, Y.; Zhao, T.; Liang, Z. Effect of polymer binders in anode catalyst layer on performance of alkaline direct ethanol fuel cells. *J. Power Sources.* **2009**, *190*, 223–229. [CrossRef]

64. Su, H.; Pasupathi, S.; Bladergroen, B.; Linkov, V.; Pollet, B. Optimization of gas diffusion electrode for polybenzimidazole-based high temperature proton exchange membrane fuel cell: Evaluation of polymer binders in catalyst layer. *Int. J. Hydrog. Energy* **2013**, *38*, 11370–11378. [CrossRef]

65. Wang, W.; Duan, J.; Liu, Y.; Zhai, T. Structural Reconstruction of Catalysts in Electroreduction Reaction: Identifying, Understanding, and Manipulating. *Adv. Mater.* **2022**, 2110699. [CrossRef]

66. Chen, J.; Wang, L. Effects of the Catalyst Dynamic Changes and Influence of the Reaction Environment on the Performance of Electrochemical CO_2 Reduction. *Adv. Mater.* **2022**, *34*, 2103900. [CrossRef]

67. Woldu, A.; Huang, Z.; Zhao, P.; Hu, L.; Astruc, D. Electrochemical CO_2 reduction (CO_2RR) to multi-carbon products over copper-based catalysts. *Coord. Chem. Rev.* **2022**, *454*, 214340. [CrossRef]

68. Todorova, T.; Schreiber, M.; Fontecave, M. Mechanistic Understanding of CO_2 Reduction Reaction (CO_2RR) Toward Multicarbon Products by Heterogeneous Copper-Based Catalysts. *ACS Catal.* **2020**, *10*, 1754–1768. [CrossRef]

69. Kim, Y.-G.; Baricuatro, J.; Javier, A.; Gregoire, J.; Soriaga, M. The Evolution of the Polycrystalline Copper Surface, First to Cu(111) and Then to Cu(100), at a Fixed CO_2RR Potential: A Study by Operando EC-STM. *Langmuir* **2014**, *30*, 15053–15056. [CrossRef]

70. Tian, Z.; Priest, C.; Chen, L. Recent Progress in the Theoretical Investigation of Electrocatalytic Reduction of CO_2. Adv. *Theory Simul.* **2018**, *1*, 1800004. [CrossRef]

71. Li, Q.; Guo, Y.; Tian, Y.; Liu, W.; Chu, K. Activating VS_2 basal planes for enhanced NRR electrocatalysis: The synergistic role of S-vacancies and B dopants. *J. Mater. Chem. A* **2020**, *8*, 16195–16202. [CrossRef]

72. Li, X.; Tian, Y.; Wang, X.; Guo, Y.; Chu, K. $SnNb_2O_6$ nanosheets for the electrocatalytic NRR: Dual-active-center mechanism of Nb_{3c} and Sn_{4c}–Nb_{5c} dimer. *Sustain. Energy Fuels* **2021**, *5*, 4277–4283. [CrossRef]

73. Liu, A.; Yang, Y.; Kong, D.; Ren, X.; Gao, M.; Liang, X.; Yang, Q.; Zhang, J.; Gao, L.; Ma, T. DFT study of the defective carbon materials with vacancy and heteroatom as catalyst for NRR. *Appl. Surf. Sci.* **2021**, *536*, 147851. [CrossRef]

74. Cai, W.; Han, Y.; Pan, Y.; Zhang, X.; Xu, J.; Zhang, Y.; Sun, Y.; Li, S.; Lai, J.; Wang, L. The twinned Pd nanocatalyst exhibits sustainable NRR electrocatalytic performance by promoting the desorption of NH3. *J. Mater. Chem. A* **2021**, *9*, 13483–13489. [CrossRef]

75. Reier, T.; Oezaslan, M.; Strasser, P. Electrocatalytic Oxygen Evolution Reaction (OER) on Ru, Ir, and Pt Catalysts: A Comparative Study of Nanoparticles and Bulk Materials. *ACS Catal.* **2012**, *2*, 1765–1772. [CrossRef]

76. Anantharaj, S.; Kundu, S.; Noda, S. "The Fe Effect": A review unveiling the critical roles of Fe in enhancing OER activity of Ni and Co based catalysts. *Nano Energy* **2021**, *80*, 105514. [CrossRef]

77. Yao, N.; Wang, G.; Jia, H.; Yin, J.; Cong, H.; Chen, S.; Luo, W. Intermolecular Energy Gap-Induced Formation of High-Valent Cobalt Species in CoOOH Surface Layer on Cobalt Sulfides for Efficient Water Oxidation. *Angew. Chem. Int. Ed.* **2022**, *61*, e202117178. [CrossRef]

78. Chen, Y.; Sun, Y.; Wang, M.; Wang, J.; Li, H.; Xi, S.; Wei, C.; Xi, P.; Sterbinsky, G.; Freeland, J.; et al. Lattice site-dependent metal leaching in perovskites toward a honeycomb-like water oxidation catalyst. *Sci. Adv.* **2021**, *7*, eabk1788. [CrossRef]

79. Wang, C.-P.; Feng, Y.; Sun, H.; Wang, Y.; Yin, J.; Yao, Z.; Bu, X.-H.; Zhu, J. Self-Optimized Metal–Organic Framework Electrocatalysts with Structural Stability and High Current Tolerance for Water Oxidation. *ACS Catal.* **2021**, *11*, 7132–7143. [CrossRef]

80. Dupin, J.-C.; Gonbeau, D.; Vinatier, P.; Levasseur, A. Systematic XPS studies of metal oxides, hydroxides and peroxides. *Phys. Chem. Chem. Phys.* **2000**, *2*, 1319–1324. [CrossRef]

81. Karthikeyan, M.; Mahapatra, D.; Razak, A.; Abahussain, A.; Ethiraj, B.; Singh, L. Machine learning aided synthesis and screening of HER catalyst: Present developments and prospects. *Cat. Rev.* **2022**, 1–31. [CrossRef]

82. Back, S.; Tran, K.; Ulissi, Z. Toward a Design of Active Oxygen Evolution Catalysts: Insights from Automated Density Functional Theory Calculations and Machine Learning. *ACS Catal.* **2019**, *9*, 7651–7659. [CrossRef]

83. Wang, P.; Li, H.; Hu, B.; Sun, Y.; Huang, R.; Liu, L. Spin-state reconfiguration induced by alternating magnetic field for efficient oxygen evolution reaction. *Nat. Commun.* **2021**, *12*, 4827.

84. Li, T.; Huang, R.; Wang, P.; Hu, B.; Li, H.; Liu, L.; Sun, Y. Recharged catalyst with memristive nitrogen reduction activity through learning networks of spiking neurons. *J. Am. Chem. Soc.* **2021**, *143*, 5378–5385.

85. Wang, P.; Hu, B.; Shen, X.; Liu, C.; Tao, W.; Huang, P. Spin-related symmetry breaking induced by half-disordered hybridization in BixEr$_{2-x}$Ru$_2$O$_7$ pyrochlores for acidic oxygen evolution. *Nat. Commun.* **2022**, *13*, 4106.

86. He, J.; Liu, F.; Chen, Y.; Liu, X.; Zhang, X.; Zhao, L.; Chang, B.; Wang, J.; Liu, H.; Zhou, W. Cathode electrochemically reconstructed V-doped CoO nanosheets for enhanced alkaline hydrogen evolution reaction. *Chem. Eng. J.* **2022**, *432*, 134331. [CrossRef]

87. Deng, Y.; Liu, Z.; Wang, A.; Sun, D.; Chen, Y.; Yang, L.; Pang, J.; Li, H.; Li, H.; Liu, H.; et al. Oxygen-incorporated MoX (X: S, Se or P) Nanosheets via Universal and Controlled Electrochemical Anodic Activation for Enhanced Hydrogen Evolution Activity. *Nano Energy* **2019**, *62*, 338–347. [CrossRef]

88. Sun, C.; Wang, L.; Zhao, W.; Xie, L.; Wang, J.; Li, J.; Li, B.; Liu, S.; Zhuang, Z.; Zhao, Q. Atomic-Level Design of Active Site on Two-Dimensional MoS$_2$ toward Efficient Hydrogen Evolution: Experiment, Theory, and Artificial Intelligence Modelling. *Adv. Funct. Mater.* **2022**, *38*, 2206163. [CrossRef]

89. Chang, C.; Wang, L.; Xie, L.; Zhao, W.; Liu, S.; Zhuang, Z.; Liu, S.; Li, J.; Liu, X. Amorphous molybdenum sulfide and its Mo-S motifs: Structural characteristics, synthetic strategies, and comprehensive applications. *Nano Res.* **2022**, *15*, 8613–8635. [CrossRef]

90. Jing, C.; Tang, Y.; Wang, S.; Xie, L.; Chang, C.; Cheng, X.; Liu, M.; Wang, L.; Wang, L. Ingeniously designed Ni-Mo-S/ZnIn$_2$S$_4$ composite for multi-photocatalytic reaction systems. *Chinese Chem. Lett.* **2022**, *3*, 1468–1474.

91. Tang, M.; Yin, W.; Liu, S.; Yu, H.; He, Y.; Cai, Y.; Wang, L. Sulfur Line Vacancies in MoS$_2$ for Catalytic Hydrogen Evolution Reaction. *Crystals* **2022**, *12*, 1218. [CrossRef]

92. Wang, S.; Wang, L.; Xie, L.; Zhao, W.; Liu, X.; Zhuang, Z.; Zhuang, Y.; Chen, J.; Liu, S. Dislocation-strained MoS2 nanosheets for high-efficiency hydrogen evolution reaction. *Nano Res.* **2022**, *15*, 4996–5003. [CrossRef]

93. Cheng, X.; Wang, L.; Xie, L.; Sun, C.; Zhao, W.; Liu, X.; Zhuang, Z.; Liu, S.; Zhao, Q. Defect-driven selective oxidation of MoS2 nanosheets with photothermal effect for Photo-Catalytic hydrogen evolution reaction. *Chem. Eng. J.* **2022**, *439*, 135757. [CrossRef]